

LASER INDUCED GRATING SPECTROSCOPY OF
RARE EARTH IONS IN SOLIDS

By

VALENTINA ADELAIDA FRENCH

Master of Science

Oklahoma State University

Stillwater, Oklahoma

1987

Submitted to the Faculty of the
Graduate College of the
Oklahoma State University
in partial fulfillment of
the requirements for
the Degree of
DOCTOR OF PHILOSOPHY
December, 1992

Thesis
1992D
F876L

LASER INDUCED GRATING SPECTROSCOPY OF
RARE EARTH IONS IN SOLIDS

Thesis Approved:

Richard C. Powell

Thesis Adviser

Paul Werthaus

Bruce Welfer

James Soy

Edward T. Knoble

Thomas C. Collins

Dean of the Graduate College

ACKNOWLEDGMENTS

I wish to express my gratitude to my thesis adviser, Dr. Richard C. Powell, for giving me the opportunity to learn and work in his laboratory and for his help, guidance and continuous support throughout this work. Special thanks and appreciation are also extended to the other PhD Advisory Committee members, Dr. George Dixon, Dr. Paul Westhaus, Dr. J.J. Song and Dr. Edward Knobbe for their kind cooperation.

I would like to express my appreciation to Dr. Roger Reeves, Dr. Huimin Liu, Dr. Istvan Foldvari, Roger Petrin, Keith Ver Steeg and Dr. Antonio Munoz for their assistance in the laboratory.

I want to thank my mother and my family for their love and constant support. My special thanks go to my husband, Robert, whose love, patience, understanding, help, encouragement and support have made all of this possible. I want to thank God for giving me the strength and ability to complete this work.

I gratefully acknowledge the financial support provided by the U.S. Department of Education Fellowship in Areas of National Needs. I also acknowledge the U.S. Army Research Office and the National Science Foundation for providing funding for this research.

TABLE OF CONTENTS

| Chapter | Page |
|----------------------------------------------------------------------------------------|------|
| I. INTRODUCTION | 1 |
| Summary of Thesis | 1 |
| II. ENERGY TRANSFER PROCESSES IN RARE EARTH DOPED YAG CRYSTALS | 3 |
| Introduction | 3 |
| Theoretical Background | 5 |
| Single-Step Resonant Energy Transfer | 8 |
| Multistep Energy Transfer | 15 |
| Time-Resolved Fluorescence Spectroscopy | 20 |
| Samples and Experimental Procedure | 20 |
| Experimental Results and Interpretation | 23 |
| Transient Laser-Induced Grating Spectroscopy | 35 |
| Theoretical Background | 36 |
| Experimental Procedure | 42 |
| Experimental Results and Interpretation | 44 |
| Discussion | 56 |
| III. REFRACTIVE INDEX GRATINGS IN RARE EARTH DOPED ALKALINE EARTH GLASSES | 60 |
| Introduction | 60 |
| Experimental Procedure and Results | 61 |
| Interpretation of Results | 65 |
| Discussion | 75 |
| IV. CONCLUSIONS | 77 |
| BIBLIOGRAPHY | 80 |

LIST OF TABLES

| Table | | Page |
|-------|------------------------------------------------------------------------------------------|------|
| I. | Concentrations of samples used for energy transfer studies | 21 |
| II. | Critical interaction distances calculated in this work | 32 |
| III. | Ion-ion interaction rate and excitation scattering rate at room temperature | 47 |
| IV. | Excitation migration parameters at room temperature | 50 |
| V. | Composition of glass samples investigated | 62 |
| VI. | Double minimum potential well parameters | 71 |

LIST OF FIGURES

| Figure | Page |
|-----------------------------------------------------------------------------------------------------------------------------------------------------------------------------------|------|
| 1. Energy transfer processes in Tm,Ho:YAG | 4 |
| 2. Diagram of the rare earth ions energy levels relevant in this work | 6 |
| 3. Energy transfer and migration processes investigated in this work | 7 |
| 4. Experimental setup for time-resolved fluorescence spectroscopy | 22 |
| 5. Normalized emission and absorption spectra of the transitions involving the Tm 3F_4 level at room temperature | 24 |
| 6. Normalized emission and absorption spectra of the transitions involving the Tm 3F_4 and Ho 5I_7 energy levels, respectively, at room temperature | 25 |
| 7. Normalized emission and absorption spectra of the transitions involving the Tm 3F_4 level at a temperature of 12 K | 27 |
| 8. Fluorescence from the Tm 3F_4 level and the Ho 5I_7 level in Tm,Ho:YAG at room temperature | 28 |
| 9. Rise of the fluorescence emission from the Ho 5I_7 level in Tm,Ho:YAG at room temperature after pumping the Tm ions | 29 |
| 10. Fluorescence emission decay pattern from the Tm 3F_4 level in sample 4 at room temperature | 30 |
| 11. Normalized emission and absorption spectra of the transitions involving the Tm 3F_4 and Er $^4I_{13/2}$ energy levels, respec- tively, at room temperature | 31 |
| 12. Nonradiative cross-relaxation between two systems of ions, D and A | 33 |

| Figure | Page |
|----------------------------------------------------------------------------------------------------------------------------------------------------------------------------------------------|------|
| 13. Experimental setup for nondegenerate four-wave-mixing | 43 |
| 14. LIG transient decay pattern from sample 1 at room temperature . . . | 46 |
| 15. Variation of the ion-ion interaction rate with Tm concentration | 49 |
| 16. Variation of the ion-ion interaction rate with temperature for sample 1 | 52 |
| 17. Variation of the excitation scattering rate with temperature for sample 1 | 54 |
| 18. Variation of the diffusion coefficient with Tm concentration at room temperature | 55 |
| 19. Absorption spectrum of Cr,Tm,Er:YAG at room temperature | 58 |
| 20. Fluorescence emission spectrum of Cr,Tm,Er:YAG at room temperature | 59 |
| 21. Scattering efficiency of the laser-induced permanent gratings versus the reduced mass of the modifier and the rare earth ion . . . | 63 |
| 22. Intensity of the laser-induced signal in the Mg glass sample as a function of temperature | 64 |
| 23. Diagram of the Eu^{3+} ion energy levels and relaxation processes relevant in this work | 66 |
| 24. Double-minimum potential well model | 67 |
| 25. Configuration coordinate diagram showing the relevant energy levels of the Eu^{3+} ion with the two possible local configura- tions of the glass host, I and II | 74 |

CHAPTER I

INTRODUCTION

Laser spectroscopy is an important tool in investigating the optical properties of solids, including the study of higher energy electronic excited states, radiationless decay processes, multiphoton transitions and energy transfer processes. Understanding and characterizing the optical properties of materials is important in determining their potential use in high technology applications.

Summary of Thesis

The work presented in this thesis makes use of laser spectroscopy techniques to study the optical properties of some rare-earth-doped laser crystals and of Eu-doped silicate glasses.

In the second chapter the results of a study of energy transfer and migration processes in Tm,Ho:YAG, Tm:YAG and Cr,Tm,Er:YAG crystals are presented. Energy transfer processes can enhance laser performance by increasing the pumping efficiency of the active ions, but can also decrease the efficiency of laser operation through concentration quenching mechanisms. Characterizing energy transfer is thus important in developing efficient laser materials. Laser-induced grating spectroscopy was used to study spatial migration of energy among the Tm ions as a function of both temperature and Tm ion concentration. Efficient long range energy migration was found to take place in the 3F_4 level, which enhances the energy transfer to Ho^{3+} ions. The parameters describing excitation migration were determined experimentally and used to calculate an overall Tm-Ho energy transfer rate. This was found to be in close agreement with the rate determined by

the results of fluorescence spectral dynamics measurements. Theoretical estimates were made of the fundamental ion-ion interaction rates responsible for each of the physical processes investigated here and the results were all found to be in close agreement with the experimentally determined values.

The third chapter describes the results of an investigation using four-wave-mixing techniques to produce permanent laser-induced refractive index gratings in Eu^{3+} -doped silicate glasses. These gratings are associated with a thermally induced change in the local glass structure at the site of the Eu^{3+} ions, leading to a double-minimum potential well for the electronic energy levels of the Eu^{3+} ions. The effects on the characteristics of the permanent laser-induced gratings produced by changing the divalent modifier ions of the glass host are reported and a theoretical model is presented to explain the physical origin of the change in the refractive index of the material.

In the fourth chapter a summary of results and conclusions are presented.

CHAPTER II

ENERGY TRANSFER PROCESSES IN RARE EARTH DOPED YAG CRYSTALS

Introduction

The development of room temperature lasers based on $\text{Y}_3\text{Al}_5\text{O}_{12}:\text{Tm}^{3+}, \text{Ho}^{3+}$ (Tm,Ho:YAG) crystals has led to a renewed interest in the optical properties of this material. As a result, a significant amount of work has been done in recent years on measuring the spectroscopic and lasing properties of the Tm,Ho:YAG system [1–5]. The previous research has identified a complex chain of physical processes by which the pump photon energy is transferred from the Tm^{3+} to the Ho^{3+} ions. These processes are shown in Figure 1. In a diode laser-pumped Tm,Ho:YAG laser, the $^3\text{H}_4$ level of the Tm ions is directly excited by the pump energy. This is followed by a cross-relaxation process between neighboring Tm ions which gives rise to two Tm ions in the $^3\text{F}_4$ level for each photon absorbed in the $^3\text{H}_4$ level. This process increases the efficiency of energy transfer from the Tm^{3+} to the Ho^{3+} ions. There is spatial energy migration among the Tm ions in the $^3\text{F}_4$ level followed by direct transfer of energy from this level to the Ho $^5\text{I}_7$ level [1]. It has also been suggested that an additional spatial energy migration process may occur in the $^3\text{H}_4$ level of the Tm ions in samples of high Tm concentration [2]. The properties of these complex processes have not been well characterized. Previous studies focused on the initial Tm cross-relaxation process [3] or on the overall Tm-Ho energy transfer efficiency [6,7]. A detailed understanding of the energy transfer processes in Tm,Ho:YAG crystals is important for modeling the optical pumping dynamics of these lasers in order to understand their operational properties and to optimize dopant concentrations to increase the efficiency of laser operation.

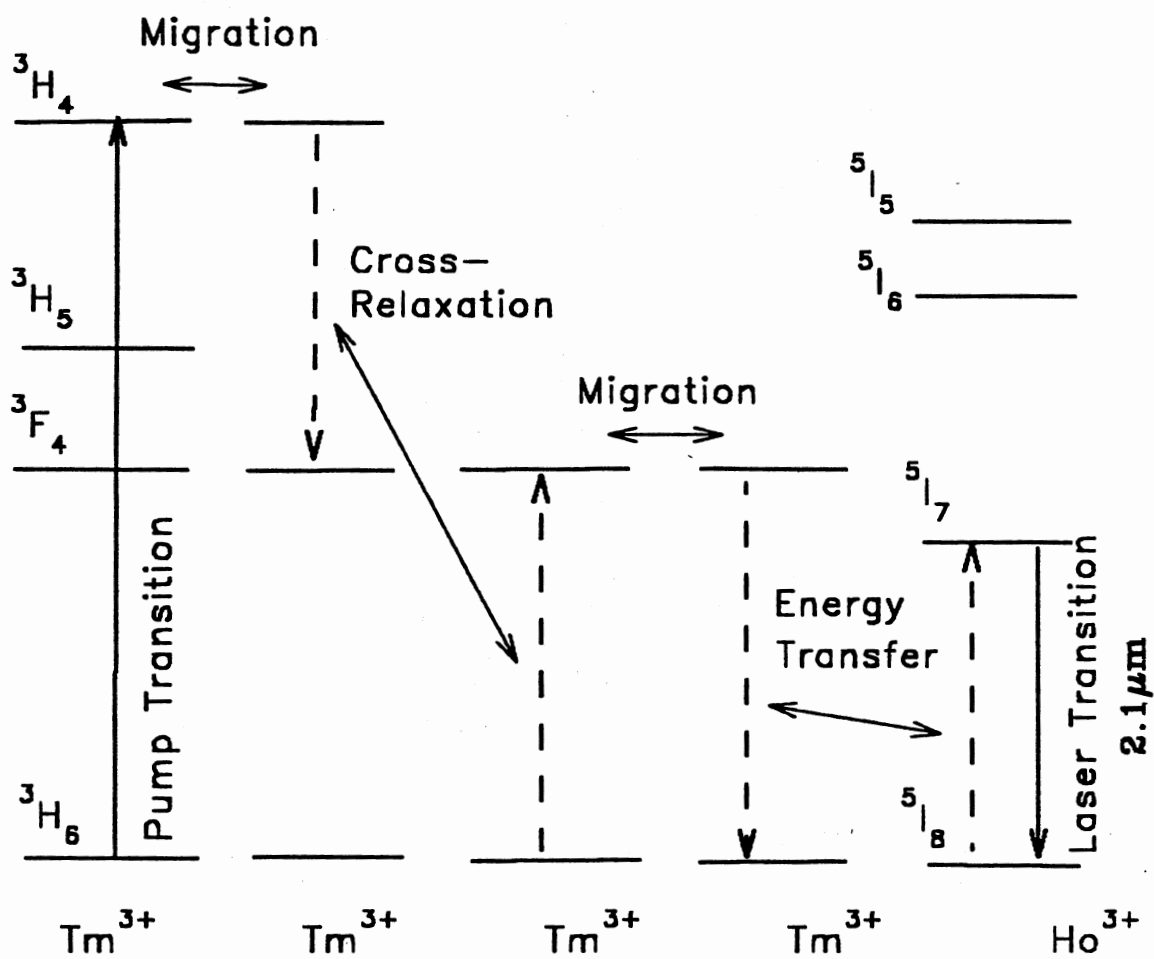


Figure 1. Energy transfer processes in Tm,Ho:YAG.

Reported in this chapter are the results of a study of energy transfer and migration processes in Tm,Ho:YAG and Tm:YAG and Cr,Tm,Er:YAG laser crystals using both time-resolved and laser-induced grating spectroscopy. Figure 2 shows the relevant energy levels of the Tm, Ho and Er ions and Figure 3 shows the processes investigated in this work. Special consideration is given to the energy migration processes, which have received little attention in previous research. The fundamental properties of these processes can be accurately explained through theoretical models of ion-ion interaction mechanisms. The overall Tm-Ho energy transfer rate predicted as a result of sequential relaxation, migration, and trapping processes is shown to be consistent with the experimentally measured values.

Theoretical Background

When a material is exposed to light, energy may be absorbed through the creation of electronic excited states. The optically active ions that absorb this energy are called donors (D) or sensitizers. Later, this energy may be emitted in the form of light or heat by ions other than those initially excited. These latter ions are called acceptors (A) or activators. The movement of excitation energy from the donors to the acceptors is called "energy transfer". "Radiationless energy transfer" between ions may be thought of as a quantum mechanical resonance process involving the exchange of a virtual photon [8]. The transfer mechanism can be either an electromagnetic multipole-multipole interaction or an exchange interaction. Whenever an excited donor transfers its energy directly to an acceptor in the ground state, the transfer process is called "single-step energy transfer". If the transitions of the donor and acceptor ions occur at very nearly the same frequency, the energy transfer process is resonant. When a mismatch in energy between the transitions of D and A ions exists, D→A energy transfer can occur through phonon-assisted processes. In situations when the donor concentration is much higher than the acceptor concentration, the excitation energy migrates many times between donors before transfer to an acceptor occurs. This process is known as "multistep energy transfer".

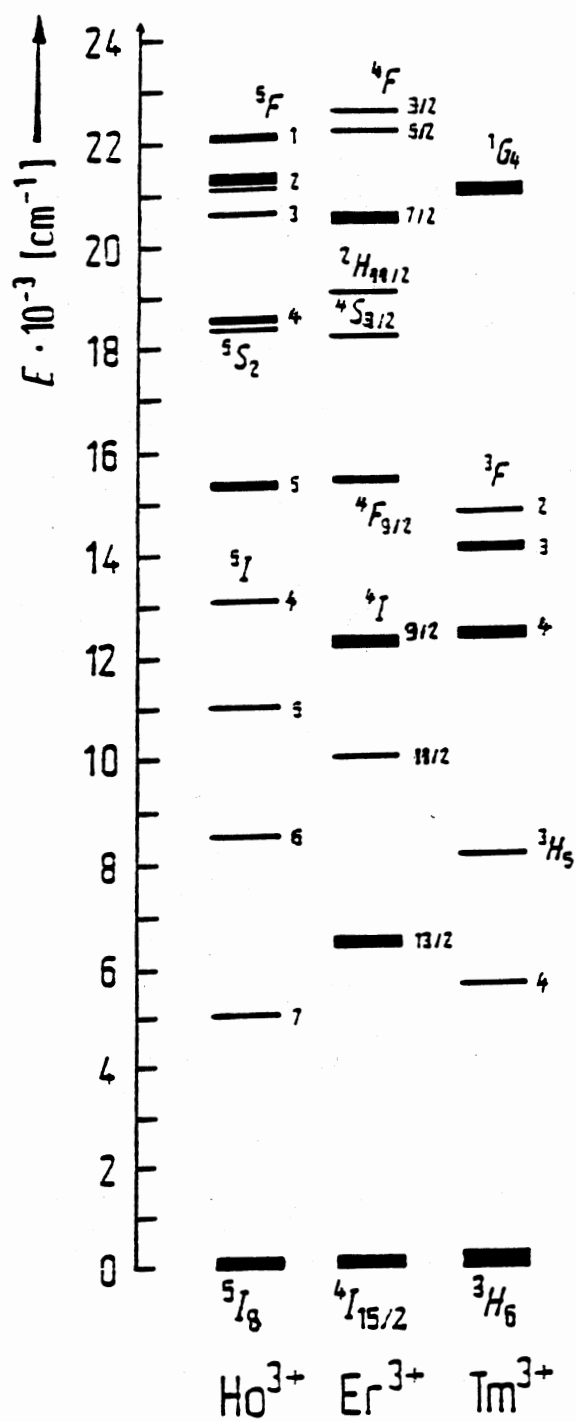


Figure 2. Diagram of the rare earth ions energy levels relevant in this work

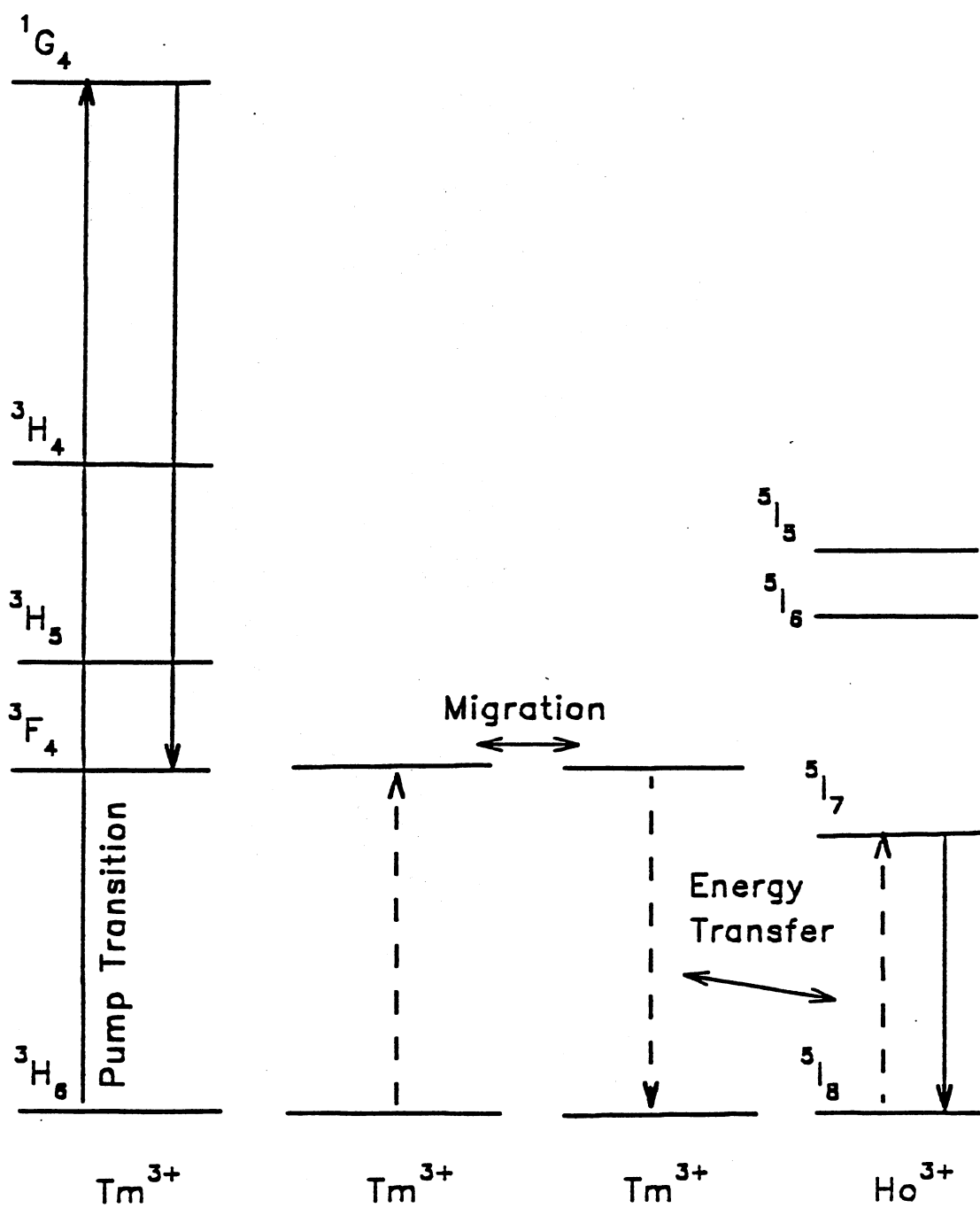


Figure 3. Energy transfer and migration processes investigated in this work

Single-Step Resonant Energy Transfer

The electromagnetic interaction between a donor ion, D, and an acceptor ion, A, is responsible for the nonradiative energy transfer from D to A. The theory of transfer via electric dipole-dipole interaction was first developed by Forster [9] and later by Dexter [10] who expanded the treatment to multipole-multipole and to exchange interactions.

Consider a donor ion, D, initially in the excited state, ψ'_D , and an acceptor ion, A, in the ground state, ψ_A . The primed quantities in this section will refer to excited states. The electrostatic Coulomb interaction between the electrons of the two ions is given by [11]

$$H_{DA} = \frac{1}{2} \sum_{i,j} \frac{e^2/\epsilon}{|\vec{r}_{D_i} - \vec{r}_{A_j} - \vec{R}_{DA}|} \quad (1)$$

Here \vec{r}_{D_i} and \vec{r}_{A_j} represent the positions of the electrons i and j belonging to ions D and A, respectively, \vec{R}_{DA} is the donor-acceptor separation (the distance between the nuclei of D and A), the sum is over the electrons of the two ions and ϵ is the dielectric constant of the host crystal. This interaction, also called Van der Waals' interaction, gives rise to Van der Waals' forces in molecular systems [11]. Using a Taylor series expansion about \vec{R}_{DA} , the electrostatic interaction, H_{DA} , can be expressed as a multipole expansion, the leading terms corresponding to electric dipole-dipole, electric dipole-quadrupole and electric quadrupole-quadrupole interactions [10,11].

According to the time-dependent perturbation theory, the energy transfer rate (energy transfer probability per unit time) from D to A is given by Fermi's Golden Rule and, for resonant transfer, can be written as [10]

$$W_{DA} = \frac{2\pi}{\hbar} \rho_E |\langle \Psi_f | H_{DA} | \Psi_i \rangle|^2 \quad (2)$$

where Ψ_i and Ψ_f are the initial and final antisymmetrized wave functions of the system and ρ_E is the density of final states. Ψ_i corresponds to the case when the donor ion, D, is in the excited state, ψ'_D , and the acceptor, A, is in the ground

state, ψ_A , and Ψ_f corresponds to the case when D is in its ground state, ψ_D , while A is in the excited state, ψ'_A . Due to lattice vibrations, the initial and final levels of D and A are not well defined. The wavefunctions and the density of states can then be treated as functions of energy [10].

For a dipole-dipole interaction mechanism between D and A, the transfer rate can be written [10] as

$$W_{DA} = \frac{4\pi e^4}{3\hbar\epsilon^2 R_{DA}^6 g'_D g_A} \sum_I \sum_F \int dE \left\{ \int d\omega'_D p'_D(\omega'_D) | \langle \vec{r}_D(\omega'_D, \omega'_D - E) \rangle |^2 \right\} \times \left\{ \int d\omega_A p_A(\omega_A) | \langle \vec{r}_A(\omega_A, \omega_A + E) \rangle |^2 \right\} \quad (3)$$

where $\langle \vec{r}_D \rangle = \langle \psi'_D | \vec{r}_D | \psi_D \rangle$, $\langle \vec{r}_A \rangle = \langle \psi_A | \vec{r}_A | \psi'_A \rangle$, $p'_D(\omega'_D)$ and $p_A(\omega_A)$ represent the probability that D is in the particular state of energy ω'_D , and A is in the state of energy ω_A , respectively, g'_D and g_A are the degeneracy of the excited state of D and of the ground state of A, respectively, and

$$\omega'_D - \omega_D = \omega'_A - \omega_A = E. \quad (4)$$

The sums over I and F represent sums over all possible transitions that can contribute to the transfer, that is, sums over i_D , i_A , f_D and f_A (here i and f refer to the initial and final states of D and A ions).

The matrix elements in Equation 3 are the same as those appearing in the oscillator strengths, absorption coefficients and decay times associated with the transitions of D and A ions and can, therefore, be related to these measurable quantities.

For an electric dipole transition, the probability of emission of a photon of energy E by an ion in a crystalline medium, is given by the Einstein A coefficient [10]

$$A(E) = \sum_i \sum_f \frac{4e^2 E^3}{3\hbar^4 c^3 g'} \left(\frac{\Xi_c}{\Xi} \right)^2 n^3 \int | \langle \vec{r}_{if}(\omega', \omega' - E) \rangle |^2 p'(\omega') d\omega' \quad (5)$$

where the sum is over all transitions, n is the index of refraction of the host crystal, Ξ_c is the average value of the electric field in the crystal, Ξ is the field in the vacuum and $\langle \vec{r}_{if} \rangle = \langle \psi'_i | \vec{r} | \psi_f \rangle$, ψ'_i being the initial state and ψ_f , the final state of the

ion. The shape of the function $A(E)$ is given by the emission spectrum of the ion and

$$\int A(E) dE = \frac{1}{\tau_{rad}} \quad (6)$$

where $1/\tau_{rad}$ is the radiative decay rate of the excited state. If the normalized emission spectrum is given by the function $f(E)$, which is normalized such that

$$\int f(E) dE = 1, \quad (7)$$

then, we can write

$$A(E) = \frac{f(E)}{\tau_{rad}}. \quad (8)$$

Using Equations 5 and 8, we have

$$\sum_i \sum_f \int |\langle \vec{r}_{if}(\omega', \omega' - E) \rangle|^2 p'(\omega') d\omega' = \frac{3\hbar^4 c^3 g'}{4n^3 e^2 E^3} \left(\frac{\Xi}{\Xi_c} \right)^2 \frac{1}{\tau_{rad}} f(E). \quad (9)$$

The probability of absorption of a photon of energy E is given by the Einstein B coefficient as applied to ions in a crystal host [10]

$$B(E) = \sum_i \sum_f \frac{2\pi e^2}{3\hbar^2 g} \left(\frac{\Xi_c}{\Xi} \right)^2 \int p(\omega) d\omega |\langle \vec{r}_{if}(\omega, \omega + E) \rangle|^2. \quad (10)$$

Here $\langle \vec{r}_{if} \rangle = \langle \psi_i | \vec{r} | \psi_f' \rangle$, where ψ_i is the initial state and ψ_f' , the final state of the ion.

The absorption cross-section, defined as the ratio of the absorption coefficient (cm^{-1}) to the number density of the absorbing centers (cm^{-3}), is related to $B(E)$ by [10]

$$\sigma(E) = \frac{2\pi n \hbar E}{c} B(E). \quad (11)$$

Introducing the function $F(E)$, which represents the normalized absorption line-shape, such that

$$\sigma(E) = Q F(E), \quad (12)$$

where

$$\int F(E) dE = 1 \quad (13)$$

and Q is the area under the absorption spectrum

$$Q = \int \sigma(E) dE \quad (14)$$

and using Equations 10, 11 and 12 we get

$$\sum_i \sum_f \int p(\omega) d\omega \left| \langle \vec{r}_{if}(\omega, \omega + E) \rangle \right|^2 = \frac{3\hbar c g}{4\pi^2 e^2 n E} \left(\frac{\Xi}{\Xi_c} \right)^2 Q F(E). \quad (15)$$

Equations 9 and 15 are general and can be used for either D or A. It should be pointed out that Equation 9 is valid only when there are no interactions between the emitting ion and any other ion. If there are interactions that change the emission band shape or the decay time, then this equation is not applicable. Applying Equation 9 to the donor ion, D, and Equation 15 to the acceptor ion, A, we can rewrite Equation 3 as

$$W_{DA} = \frac{3\hbar^4 c^4 Q_A}{4\pi R_{DA}^6 n^4 \tau_D} \left(\frac{\Xi}{\sqrt{\epsilon} \Xi_c} \right)^4 \int \frac{f_D(E) F_A(E)}{E^4} dE \quad (16)$$

where τ_D is the intrinsic decay time of the donor ion, in the absence of acceptors. Since the average field strength [10] in a medium is $(\Xi_c/\Xi)^2 = 1/\epsilon$, it is common practice to approximate the electric field factor $[\Xi/(\sqrt{\epsilon}\Xi_c)]^4$ as unity and introduce a quantity R_0 defined as [8]

$$R_0^6 = \frac{3\hbar^4 c^4}{4\pi n^4} Q_A \int \frac{f_D(E) F_A(E)}{E^4} dE. \quad (17)$$

R_0 is called "critical interaction distance" and represents the distance around the excited donor ion at which the nonradiative energy transfer rate is equal to the intrinsic decay rate of the donor. The integral in Equation 17 represents "the spectral overlap integral" of the donor normalized emission spectrum, $f_D(E)$, and the acceptor normalized absorption spectrum, $F_A(E)$. Equation 17 can also be written in the equivalent form

$$R_0^6 = \frac{3\hbar^4 c^4}{4\pi n^4} Q_A \int \lambda^6 f_D(\lambda) F_A(\lambda) d\lambda \quad (18)$$

where $f_D(\lambda)$ and $F_A(\lambda)$ are normalized such that $\int f_D(\lambda) d\lambda = 1$ and $\int F_A(\lambda) d\lambda = 1$. Using Equation 18, W_{DA} can be written as

$$W_{DA} = \frac{1}{\tau_D} \left(\frac{R_0}{R_{DA}} \right)^6. \quad (19)$$

Similar expressions can be derived for the energy transfer by electric dipole-quadrupole and quadrupole-quadrupole interactions, i.e.

$$W_{DA} = \frac{1}{\tau_D} \left(\frac{R_0}{R_{DA}} \right)^n \quad (20)$$

where $n = 8, 10$ for dipole-quadrupole and quadrupole-quadrupole interactions, respectively.

In real crystals there is a random distribution of donors and acceptors. An excited donor can interact with all unexcited acceptors and, in order to account for the distribution in donor-acceptor separations, averages must be performed over the volume V of the sample.

If $\rho_i(t)$ is the probability that the donor i at position \vec{R}_i is excited at time t , following a δ -function excitation pulse at $t=0$, then the function $\rho_i(t)$ evolves in time according to the equation [12]

$$\frac{d}{dt}\rho_i(t) = \left[-\frac{1}{\tau_D} - \sum_{j=1}^{N_A} W_{DA} \left(|\vec{R}_i - \vec{R}_j| \right) \right] \rho_i(t) \quad (21)$$

where \vec{R}_j is the position of acceptor j , N_A is the total number of acceptors in the sample, $1/\tau_D$ is the donor intrinsic decay rate in the absence of acceptors and W_{DA} is the probability of D-A energy transfer per unit time. It is assumed that no A→A transfer or A→D back-transfer occurs. The solution of Equation 21 with the initial condition

$$\rho_i(0) = 1 \quad (22)$$

is given by [12]

$$\rho_i(t) = \exp \left[-\frac{t}{\tau_D} - t \sum_{j=1}^{N_A} W_{DA} \left(|\vec{R}_i - \vec{R}_j| \right) \right]. \quad (23)$$

The mode of decay described by Equation 23 depends on the particular distribution of acceptors around donor i . Let $\bar{\rho}(t)$ be the statistical average of $\rho_i(t)$ over the various possible acceptor environments. Let also $u(R)$ be the probability distribution of D-A distances R in the volume of the sample V . Assuming uniform

distributions for both donors and acceptors, u is equal to $1/V$ and $\bar{\rho}(t)$ is given by [12]

$$\begin{aligned}\bar{\rho}(t) &= e^{-\frac{t}{\tau_D}} \lim_{\substack{N_A \rightarrow \infty \\ V \rightarrow \infty}} \left[\int_V e^{-tW_{DA}(R)} u(R) d^3 \vec{R} \right]^{N_A} \\ &= e^{-\frac{t}{\tau_D}} \lim_{\substack{N_A \rightarrow \infty \\ V \rightarrow \infty}} \left[\frac{4\pi}{V} \int_0^{R_V} e^{-tW_{DA}(R)} R^2 dR \right]^{N_A} \\ &= e^{-\frac{t}{\tau_D}} \lim_{\substack{N_A \rightarrow \infty \\ V \rightarrow \infty}} [I(t)]^{N_A}\end{aligned}\quad (24)$$

where $V = (4/3)\pi R_V^3$ and

$$I(t) = \frac{4\pi}{V} \int_0^{R_V} e^{-tW_{DA}(R)} R^2 dR. \quad (25)$$

The limit in Equation 24 is taken for a large solid, but in such a way that N_A/V remains constant. In order to calculate $\bar{\rho}(t)$ we need to know the function $W_{DA}(R)$. For multipole-multipole energy transfer mechanisms, $W_{DA}(R)$ is given by Equation 20. In this case $I(t)$ can be written as

$$I_n(t) = \frac{4\pi}{V} \int_{R_m}^{R_V} R^2 dR \exp \left[- \left(\frac{R_0}{R} \right)^n \frac{t}{\tau_D} \right] \quad (26)$$

where R_m is the smallest possible D-A spacing and n is the multipole order. Making a change of variables $x = (R_0/R)^n t / \tau_D$ in Equation 26 and integrating by parts we get [13]

$$I_n = 1 - x_V^{3/n} \left[\Gamma \left(1 - \frac{3}{n} \right) + \left(\frac{3}{n} \right) x_m^{-1} \exp(-x_m) \right] \quad (27)$$

where $\Gamma(c)$ is the gamma function,

$$x_V = \left(\frac{R_0}{R_V} \right)^n \frac{t}{\tau_D} \quad (28)$$

and

$$x_m = \left(\frac{R_0}{R_m} \right)^n \frac{t}{\tau_D}. \quad (29)$$

For $x_m \gg 1$ the second term in the bracket can be neglected compared with the first term. This approximation means $t/\tau_D \gg (R_m/R_0)^n$ and may be good even at very short times since R_0 is generally several times larger than R_m [13]. In this limit, we can write

$$[I_n(t)]^{N_A} = \left[1 - \left(\frac{1}{N_A} \right) N_A \left(\frac{R_0}{R_V} \right)^3 \Gamma \left(1 - \frac{3}{n} \right) \left(\frac{t}{\tau_D} \right)^{3/n} \right]^{N_A}. \quad (30)$$

If $N_A \rightarrow \infty$, $R_V \rightarrow \infty$ and the concentration of acceptors, $c_A = N_A / (4\pi R_V^3/3) = \text{const.}$, Equation 30 becomes [13]

$$[I_n(t)]^{N_A} \rightarrow \exp \left[-\frac{c_A}{c_0} \Gamma \left(1 - \frac{3}{n} \right) \left(\frac{t}{\tau_D} \right)^{3/n} \right] \quad (31)$$

and using Equation 24, $\bar{\rho}(t)$ is given by

$$\bar{\rho}(t) = \exp \left[-\frac{t}{\tau_D} - \frac{c_A}{c_0} \Gamma \left(1 - \frac{3}{n} \right) \left(\frac{t}{\tau_D} \right)^{3/n} \right]. \quad (32)$$

Here c_0 is the critical concentration defined by

$$(c_0)^{-1} = \frac{4\pi R_0^3}{3}. \quad (33)$$

The number of excited donors, $n_D(t)$, obeys a similar equation

$$n_D(t) = n_D(0) \exp \left[-\frac{t}{\tau_D} - \frac{c_A}{c_0} \Gamma \left(1 - \frac{3}{n} \right) \left(\frac{t}{\tau_D} \right)^{3/n} \right]. \quad (34)$$

The intensity of fluorescence from the donors, which represents the quantity of direct experimental interest, is proportional to $n_D(t)$ and, therefore, evolves in time in a similar way

$$\varphi(t) = \varphi(0) \exp \left[-\frac{t}{\tau_D} - \frac{c_A}{c_0} \Gamma \left(1 - \frac{3}{n} \right) \left(\frac{t}{\tau_D} \right)^{3/n} \right]. \quad (35)$$

Equation 32 was first derived by Forster [9] for a dipole-dipole interaction mechanism between D and A (i.e. $n=6$)

$$\bar{\rho}_{dd}(t) = \exp \left[-\frac{t}{\tau_D} - \gamma t^{1/2} \right] \quad (36)$$

where

$$\gamma = \left(\frac{1}{\tau_D} \right)^{1/2} \frac{c_A}{c_0} \Gamma \left(\frac{1}{2} \right) = \frac{4}{3} (\pi)^{3/2} c_A R_0^3 \left(\frac{1}{\tau_D} \right)^{1/2}. \quad (37)$$

When $\gamma \gg (1/\tau_D)$, $\bar{\rho}_{dd}(t)$ is given by

$$\bar{\rho}_{dd}(t) = \exp \left(-\gamma t^{1/2} \right). \quad (38)$$

$\bar{\rho}_{dd}(t)$ given by Eq. 38 is known as Forster's static decay function.

Multistep Energy Transfer

Characterizing multistep energy transfer involves both describing the dynamics of the donor-donor energy migration process and describing the donor-acceptor energy trapping. To do this, it is necessary to account for both the D-D and the D-A relative separations. This problem can be treated using either a random walk model or a diffusion model [8]. In the random walk model, the excitation or "exciton" is modeled as undergoing a random walk on a three dimensional lattice of donors before becoming trapped at an acceptor site.

An approach developed by Burshtein [16] treated the energy transfer rate as a random variable in a stochastic hopping process. The excitation hops from donor to donor before being transferred to an acceptor. The population of excited donors (assuming delta function excitation at time $t=0$) obeys the equation

$$N_D(t) = N_D(0) \left\{ \bar{\rho}(t) \exp\left(-\frac{t}{\tau_0}\right) + \frac{1}{\tau_0} \int_0^t \bar{\rho}(t-t') \exp\left[-\frac{t-t'}{\tau_0}\right] N(t') dt' \right\}. \quad (39)$$

Here τ_0 is the average excitation hopping time among the donors and $\bar{\rho}(t)$ represents the probability distribution function of excited donors population in the absence of energy migration among donors and, for a multipole-multipole interaction mechanism between donors, is given by Eq. 32. Burshtein pointed out [16] that the actual modulation of the donor decay process is effected only by hops with the same, "most probable" migration rate $1/\tau_0$ (smaller rates are immaterial and larger ones do not lead to noticeable spatial displacements, and consequently do not change the acceptor surroundings around the donor). For the case when the donor-donor interaction is a dipole-dipole mechanism, the "most probable" migration rate among donors is calculated as the rate at which the Laplace transform of the Forster's static decay function (Eq. 38) for the donor-donor transfer reaches its maximum value, and is given by [16], [17]

$$\frac{1}{\tau_0} = \frac{8}{27} \pi^3 n_D^2 R_{0DD}^6 / \tau_D \quad (40)$$

where R_{0DD} is the critical interaction distance for the donor-donor transfer process.

The function $N_D(t)$ is non-exponential for t small enough that migration is unimportant. In this limit $N_D(t)$ approaches the form for the no-migration case, $\bar{\rho}(t)$. This is so because at early times only donors with nearby acceptors are decaying; time is not sufficient for the excitation to hop among the donors before being transferred to the acceptors. For large t , $N_D(t)$ decays exponentially at a rate determined by migration. At these later times the only donors that are still excited are those far away from any acceptor. The excitation first hops among donor ions until it gets to a donor near an acceptor, and then it is transferred to an acceptor. As migration becomes more rapid (i.e. τ_0^{-1} increases), the boundary between these two regions shifts to shorter times until, for sufficiently fast migration, the decay appears to be purely exponential. Burshtein showed [16,17] that, for the case when both the D-D interaction and the D-A interaction are by a dipole-dipole mechanism, at large t , $N_D(t)$ decays exponentially at a rate $\tau_D^{-1} + K_M$. Here, K_M represents the overall energy transfer rate from donors to acceptors in the presence of excitation migration among the donor ions. K_M was calculated by Burshtein for two limiting cases: $R_{0DA} \ll R_{0DD}$ and $R_{0DA} \gg R_{0DD}$, where R_{0DA} is the critical interaction distance for the D-A transfer process. The results are

$$K_M = 2 \left(\frac{2\pi}{3} \right)^{5/2} n_A n_D R_{0DA}^3 R_{0DD}^3 / \tau_D \quad (41)$$

for the case when $R_{0DA} \ll R_{0DD}$ [16,17,19], and

$$K_M = \left(\frac{1}{2} \right)^{3/4} \frac{(4\pi)^2}{3} n_A n_D R_{0DD}^{9/2} R_{0DA}^{3/2} / \tau_D \quad (42)$$

for $R_{0DA} \gg R_{0DD}$ [18,19].

Huber developed a model [20] in which the treatment of multistep energy transfer is based on a set of coupled rate equations for the donors

$$\frac{dP_n(t)}{dt} = - \left(\gamma_R + X_n + \sum_{n'} W_{nn'} \right) P_n(t) + \sum_{n'} W_{n'n} P_{n'}(t). \quad (43)$$

Here P_n is the probability that the n^{th} donor is excited at time t , $W_{nn'}$ is the transfer rate from donor n to donor n' , γ_R is the radiative decay rate of the donors, X_n is the transfer rate from a donor to a nearby acceptor. It is assumed that

the transfer rates are symmetric (i.e. $W_{nn'} = W_{n'n}$) and that there is no A→D back-transfer.

The population of excited donors can be written as

$$N_D(t) = N_D(0) \exp(-\gamma_R t) f(t) \quad (44)$$

where $N_D(0)$ represents the number of excited donors at time $t=0$, assuming delta function excitation at $t=0$, and $f(t)$ is called the "survival" function and evolves in time according to Eq. 43 with $\gamma_R = 0$. In order to obtain an expression for $N_D(t)$, the survival function must be calculated from the rate equations 43 with $\gamma_R = 0$. This constitutes a very complex problem, given the random distributions of donors and acceptors. Exact solutions for all values of the acceptor concentration can be obtained only in two limiting cases: no migration among donors and (infinitely) rapid donor-donor transfer. The first case constitutes the static limit and the result is [20]

$$f(t) = \prod_n [(1 - c_A) + c_A \exp(-X_{0n}t)]. \quad (45)$$

Here indices 0,n refer to sites on the lattice, X_{0n} is the transfer rate from a donor at site 0 to an acceptor at site n and c_A represents the fraction of lattice sites occupied at random by acceptor ions. Eq. 45 is a well-known result derived earlier by Inokuti and Hirayama [21]. In the second case (rapid transfer limit) it is assumed that all donors are in contact with one another and, for $t>0$, have an equal probability of being excited. In this case $f(t)$ is given by [20]

$$f(t) = \exp\left(-c_A \sum_n X_{0n}t\right). \quad (46)$$

In the intermediate regime (between the static and rapid transfer limits) the solution is calculated in the form of the Laplace transform of the survival function [20]

$$f(s) = \int_0^\infty dt e^{-st} f(t). \quad (47)$$

The rate equations 43 can be written, using operators, as

$$\frac{d\bar{P}(t)}{dt} = -(I\gamma_R + X)\bar{P}(t) + \Gamma\bar{P}(t) \quad (48)$$

where the matrix elements of the operators above are defined as

$$[\Gamma]_{nn'} = \delta_{nn'} \sum_{nn''} W_{nn''} - (1 - \delta_{nn'}) W_{n'n}, \quad (49)$$

$$[X]_{nn'} = X_n \delta_{nn'}, \quad (50)$$

I is the identity operator and $\overline{P}(t)$ is the column vector

$$\overline{P}(t) = \begin{pmatrix} P_1(t) \\ P_2(t) \\ . \\ . \\ P_{N_D}(t) \end{pmatrix}. \quad (51)$$

Here N_D is the total number of donor ions. Using the average-t-matrix approximation, which is a method of averaging in random systems with a small number of traps, Huber calculated $f(s)$ as [20,23]

$$f(s) = \left[s + c_A \sum_{nn'} t_{nn'}(s) \right]^{-1} \quad (52)$$

where the t-matrix obeys the equation [20,23]

$$t_{nn'}(s) = X_{0n} \delta_{nn'} - \sum_{n''} X_{0n} \langle g_{nn''}(s) \rangle t_{n''n'}(s) \quad (53)$$

in which $g(s)$ is a Green function characterizing the donor-donor excitation transfer in the absence of acceptors and is given by

$$g(s) = [sI + \Gamma]^{-1} \quad (54)$$

and $\langle g_{nn''} \rangle$ represents the configurational average of g . It must be pointed out that Eqs. 52 and 53 apply only to systems where the number of acceptors is small in comparison with the number of donors (i.e. $c_A/c_D \ll 1$, where c_D is the fraction of lattice sites occupied by donor ions).

Huber extended the results to arbitrary values of the ratio c_A/c_D by using the coherent potential approximation (CPA) [22]. In this case $f(s)$ is given by [22,23]

$$f(s) = [s + X_{CPA}(s)]^{-1} \quad (55)$$

where $X_{CPA}(s)$ is the solution of the nonlinear self-consistent equation [22]

$$\int_0^\infty \frac{dX P(X) [X - X_{CPA}(s)]}{1 + [X - X_{CPA}(s)] R(s)} = 0. \quad (56)$$

Here $P(X)$ is the normalized probability distribution function of the donor-acceptor transfer rate X , $R(s)$ is the Laplace transform of the conditional probability, $R(t)$, that a donor excited at $t=0$ is still excited at a later time t in the presence of acceptors.

From Eq. 55 the asymptotic behavior of $f(t)$ as $t \rightarrow \infty$ ($s \rightarrow 0$) is inferred as [23]

$$f(t) \sim \exp[-X_{CPA}(0)t]. \quad (57)$$

An analytic expression for $X_{CPA}(0)$ can be written only in the limit of low acceptor concentration and for the case when both D-D and D-A interactions are of dipole-dipole type [22,23]

$$X_{CPA}(0) = \frac{4}{9} \pi^{7/2} n_D n_A R_{0DA}^3 R_{0DD}^3 / \tau_D. \quad (58)$$

Equation 58 above gives an evaluation of the overall donor-acceptor transfer rate for the case of low acceptor concentration.

For the case when the D-D transfer is through a dipole-dipole mechanism, Huber derived an expression for the diffusion coefficient for excitation migration among donors, assuming the donors form a cubic lattice [20]

$$D = \frac{1}{6} \frac{R_{0DD}^6}{\tau_D} \sum_{k=1}^{N_D} \frac{1}{R_{0k}^4} \quad (59)$$

where R_{0k} is the distance from a donor at site 0 to a donor at site k . Changing to a continuum, we get

$$D = \frac{1}{6} \frac{R_{0DD}^6}{\tau_D} \int_d^\infty \frac{4\pi n_D r^2 dr}{r^4} \quad (60)$$

where d is the average donor-donor distance,

$$d = \left(\frac{3}{4\pi n_D} \right)^{1/3}. \quad (61)$$

Equations 60 and 61 give

$$D = \frac{1}{2} \left(\frac{4\pi}{3} \right)^{4/3} n_D^{4/3} \frac{R_{0DD}^6}{\tau_D} \quad (62)$$

Equation 62 represents a result obtained earlier by Trlifaj [24]. Huber pointed out [20,23] that the calculation of the diffusion constant of a disordered array of donors is a very complicated problem. For low donor concentrations ($c_D \ll 1$), $D \propto (R_{0DD}^6/\tau_D) n^{4/3}$ since D has units of (length)²/time and the length scale is set by the average distance between the donor ions, the lattice parameter being unimportant. In this case Eq. 62 constitutes a reasonable first approximation for the diffusion coefficient [20,23].

Another model for multistep energy transfer was developed by Blumen and Silbey [25]. Assuming a hopping mechanism of excitation transfer and using a standard Forster equation (Eq. 32), the authors calculated an average excitation hopping rate between donors, the probability that a hop is to an acceptor site and derived an expression for the energy trapping rate. For dipole-dipole transfer mechanisms between the donor ions and between donors and acceptors, the trapping rate is given by [25]

$$K_T = \left[\frac{4\pi}{3} \Gamma\left(\frac{1}{2}\right) \right]^2 n_D n_A R_{0DD}^3 R_{0DA}^3 / \tau_D \quad (63)$$

where $\Gamma(x)$ is the gamma function.

Time-Resolved Fluorescence Spectroscopy

Samples and Experimental Procedure

The samples used in this work were Tm:Ho:YAG, Tm:YAG, Ho:YAG, Cr,Tm,Er:YAG and Er:YAG crystals with different dopant concentrations, grown by the standard Czochralski technique. The dopant concentration of each sample is listed in Table I.

The experiments performed include the measurement of optical absorption and emission spectra, fluorescence rise time and transient fluorescence decay measurements. The experimental setup for time-resolved spectroscopy and fluorescence emission spectra is shown in Figure 4. For the emission spectra measurements an argon-ion laser tuned to the 465.8 nm line was used to resonantly excite Tm ions

TABLE I
CONCENTRATIONS OF SAMPLES USED
FOR ENERGY TRANSFER STUDIES

| Sample No. | Concentrations ($\times 10^{20} \text{cm}^{-3}$) | | | |
|------------|----------------------------------------------------|------------------|------------------|------------------|
| | Tm ³⁺ | Ho ³⁺ | Er ³⁺ | Cr ³⁺ |
| 1 | 14.1 | - | - | - |
| 2 | 8.2 | 0.69 | - | - |
| 3 | 5.6 | - | - | - |
| 4 | 0.14 | - | - | - |
| 5 | - | 0.69 | - | - |
| 6 | 8.2 | - | 0.55 | 1.4 |
| 7 | - | - | 2.7 | - |

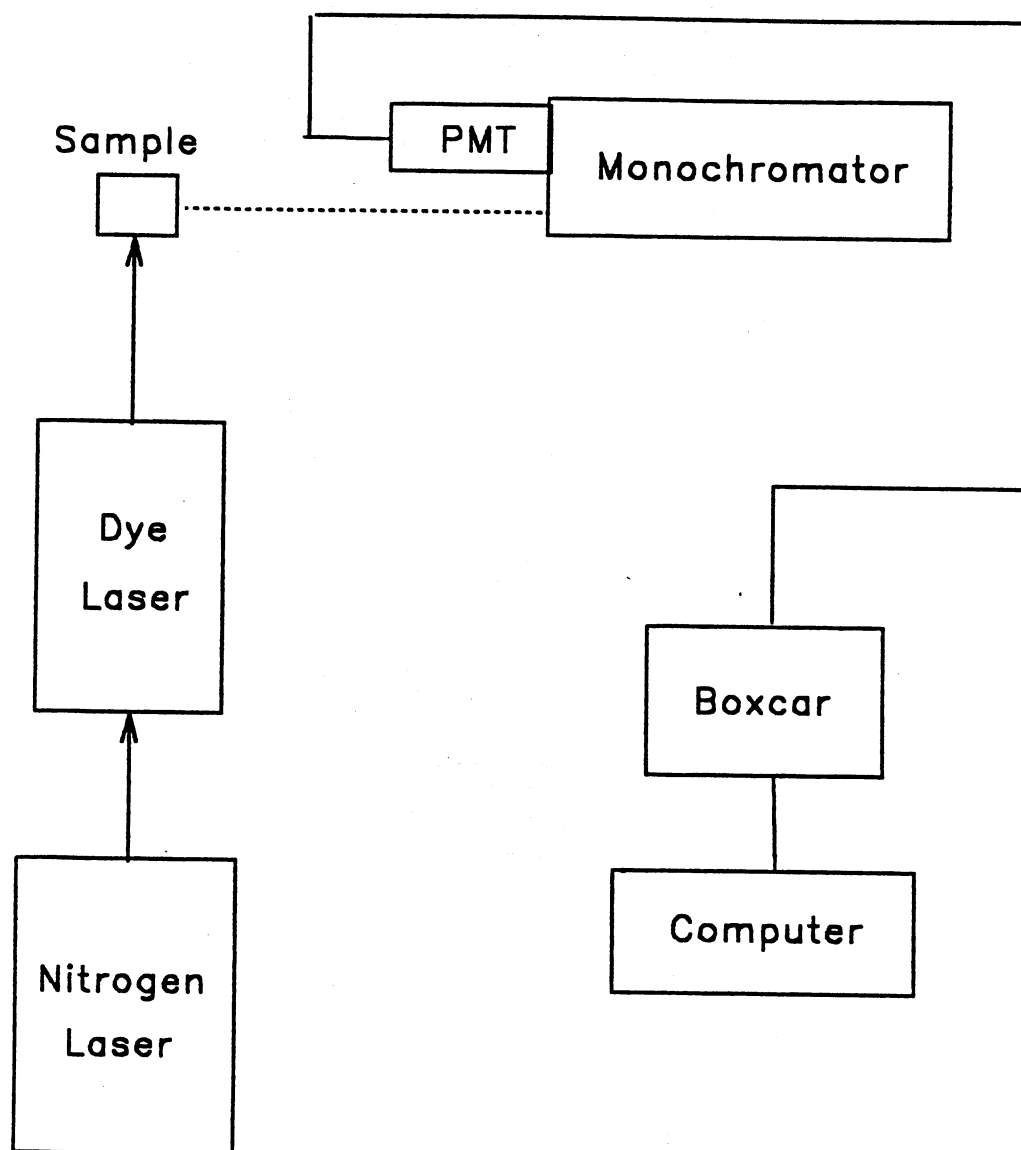


Figure 4. Experimental setup for time-resolved fluorescence spectroscopy

in the 1G_4 energy level. The excitation laser beam was focused on the sample and the resulting fluorescence was collected at a 90° angle with respect to the laser beam. The near infrared emission spectra were obtained using a 0.22 m Spex model 1681B spectrometer with gratings blazed at $1.25\ \mu\text{m}$ and $2\ \mu\text{m}$, and a PbS detector. The monochromator slit width was kept at 0.25 mm, giving a spectral resolution of $\sim 1\text{nm}$.

In the visible spectral region, emission spectra were obtained using a Spex 0.85 m double spectrometer with a 500 nm blazed grating and a Hamamatsu R446 photomultiplier tube. All emission spectra were corrected for grating and detector response. For emission rise time and transient emission decay measurements a nitrogen laser-pumped dye laser with an approximately 10 ns pulse duration was used to excite the 1G_4 level of the Tm ions. For the transient measurements in the near infrared region of the spectra, an InSb detector with a rise time of $\sim 1\ \mu\text{s}$ was used. For all fluorescence emission measurements the signal from the detector was averaged by an EG&G boxcar averager and stored on a computer.

The absorption spectra were obtained using a computer-controlled Carry 2400 spectrophotometer. For the low temperature measurements the samples were mounted in a cryostat and the temperature was controlled using a closed cycle helium refrigerator and a Lake Shore temperature controller.

Experimental Results and Interpretation

Room temperature emission and absorption spectra due to transitions associated with the 3F_4 energy level of Tm^{3+} , and absorption spectra due to transitions associated with the 5I_7 energy level of Ho^{3+} , were measured using samples 1 and 5, respectively. Figures 5 and 6 show the normalized emission and absorption spectra for these transitions. These are the spectra needed to determine the ion-ion interaction rates for energy migration among the Tm^{3+} ions in the 3F_4 level and for the Tm-Ho energy transfer.

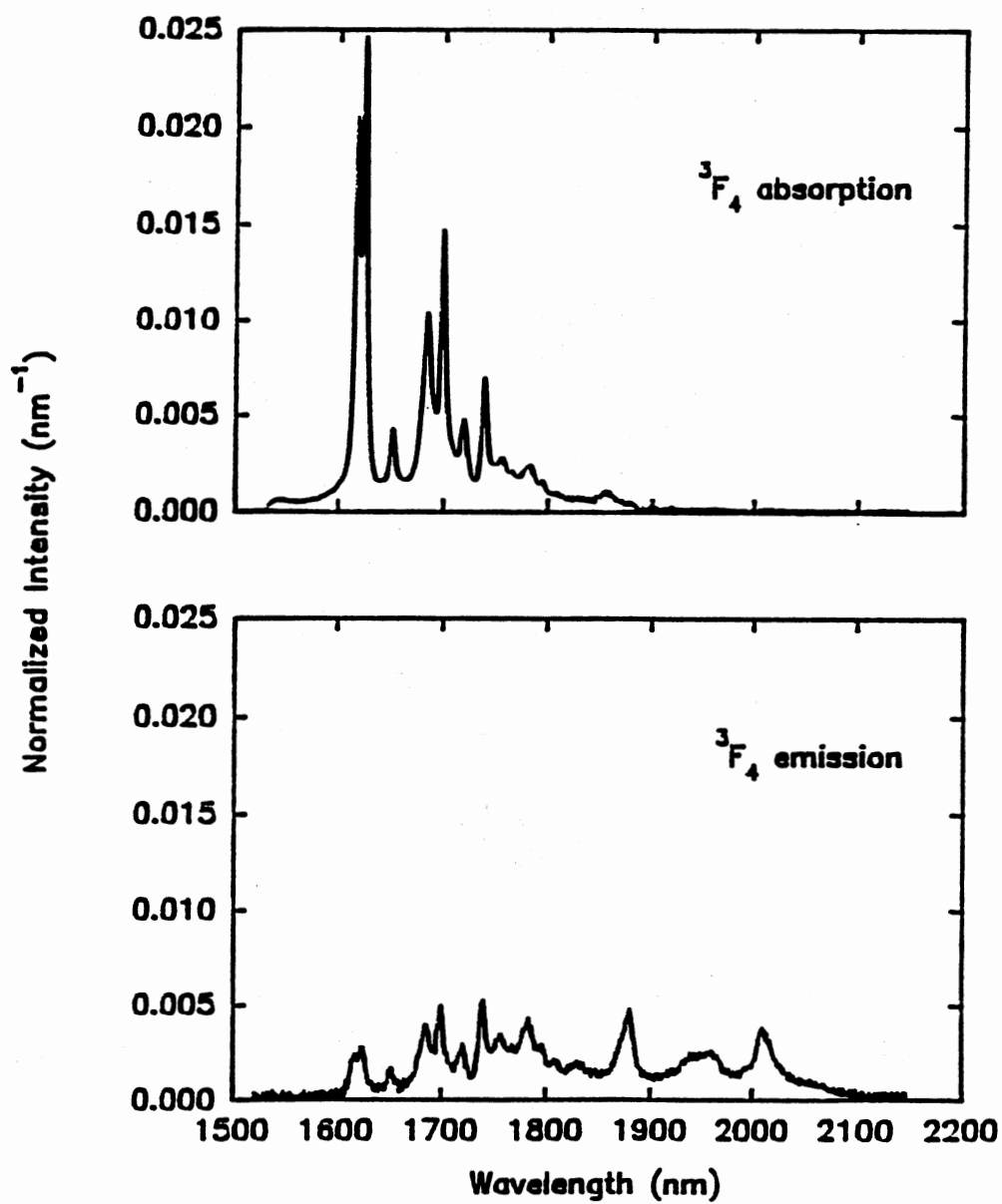


Figure 5. Normalized emission and absorption spectra of the transitions involving the Tm 3F_4 level at room temperature

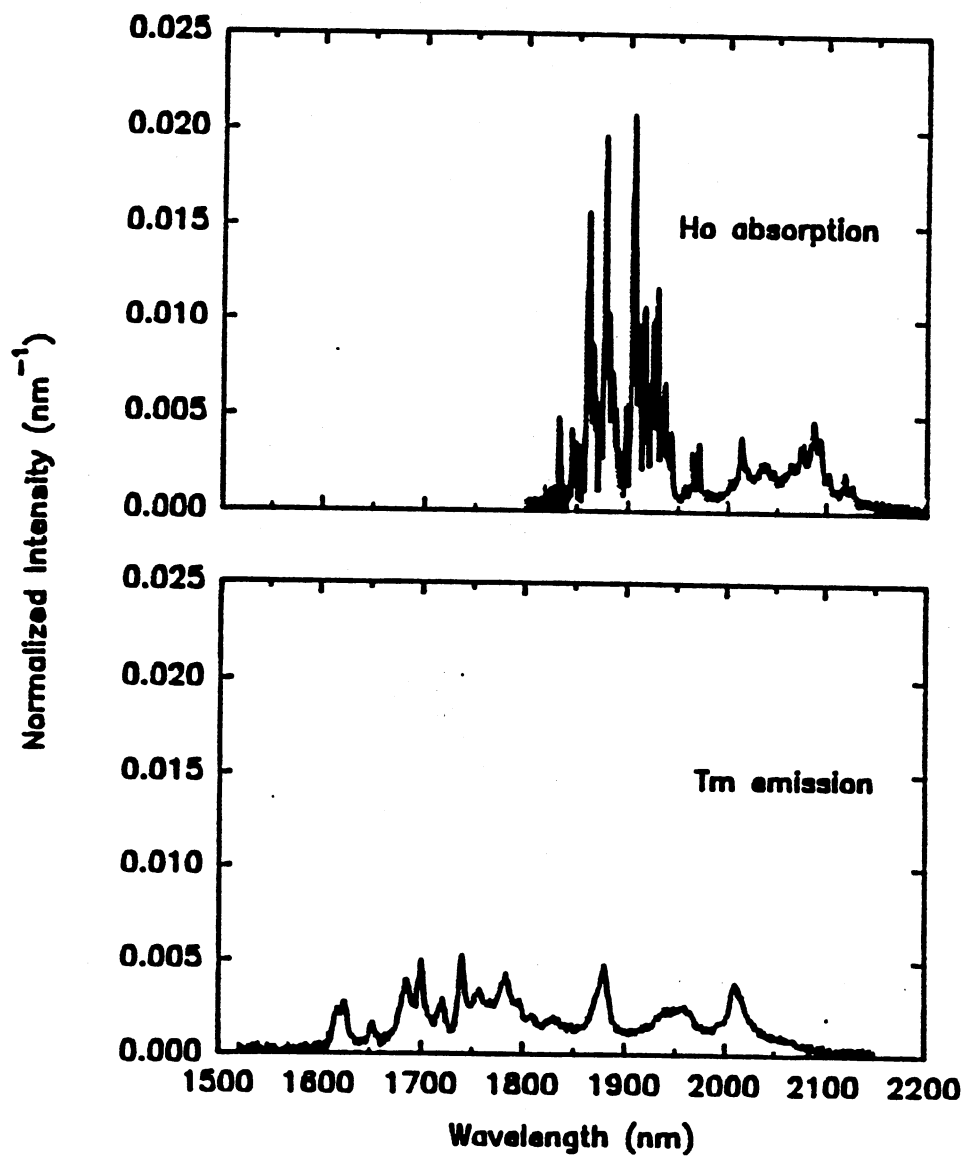


Figure 6. Normalized emission and absorption spectra of the transitions involving the Tm 3F_4 and Ho 5I_7 energy levels, respectively, at room temperature

Low temperature emission and absorption spectra associated with transitions involving the 3F_4 level of Tm^{3+} were obtained using sample 1. Figure 7 shows the normalized emission and absorption spectra of these transitions at a temperature of 12 K. These spectra are needed to understand the temperature dependence of the energy migration among Tm^{3+} ions in the 3F_4 level.

Figure 8 shows the near infrared emission from the 3F_4 and 5I_7 levels of the Tm^{3+} and Ho^{3+} ions, respectively. These spectra were measured after pumping the Tm 1G_4 energy level at room temperature using sample 2. The fluorescence decay from these metastable levels was found to be exponential in both cases with the same lifetime of ~ 6.5 ms. The rise time of the fluorescence emission from the Ho 5I_7 level is shown in Figure 9. Figure 10 shows the decay of the fluorescence from the Tm 3F_4 metastable level obtained using sample 4. As can be seen in Figure 10, the decay is exponential with a lifetime of ~ 11 ms. This value should provide a good approximation for the intrinsic lifetime of the Tm 3F_4 energy level in YAG.

Room temperature absorption spectra for transitions associated with the $^4I_{13/2}$ energy level of the Er ions were measured using sample 7. Figure 11 shows the normalized absorption spectra associated with these transitions and the normalized emission spectra for transitions between 3F_4 - 3H_6 levels of the Tm ions. These spectra are needed to calculate the ion-ion interaction rates for the Tm -Er energy transfer process.

The measured absorption and emission spectra described above can be used to calculate spectral overlap integrals needed to predict the critical interaction distances associated with the ion-ion interaction rates. Using Eq. 18 and the spectra presented above, the critical interaction distances for the Tm - Tm and Tm - Ho interaction processes were calculated. These values are listed in Table II.

An overall $Tm \rightarrow Ho$ energy transfer rate can be calculated from the results of fluorescence spectral dynamics measurements in sample 2.

Consider a nonradiative cross-relaxation process between two systems of ions, D and A, illustrated in Figure 12. The rate equations for the populations of the

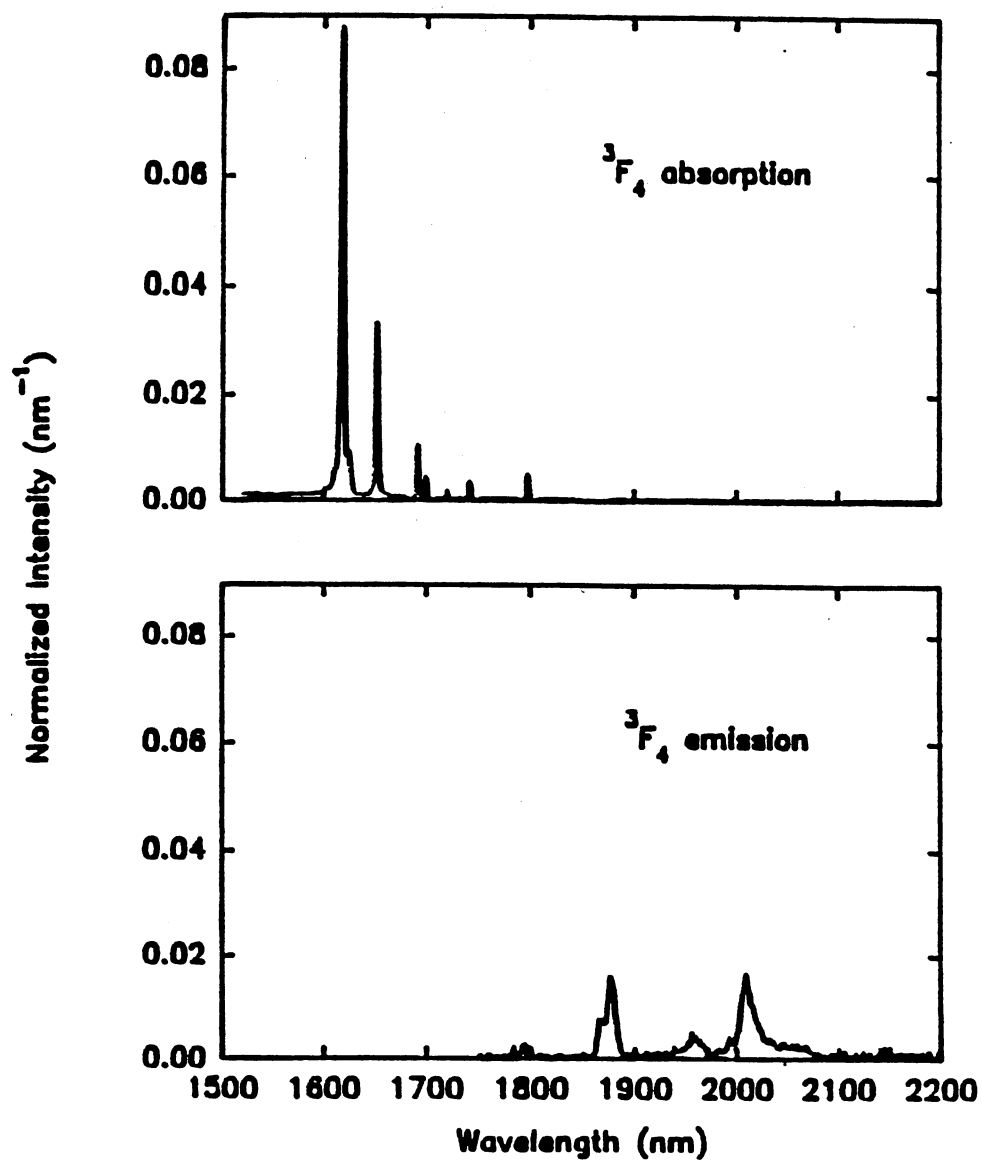


Figure 7. Normalized emission and absorption spectra of the transitions involving the Tm 3F_4 level at a temperature of 12 K

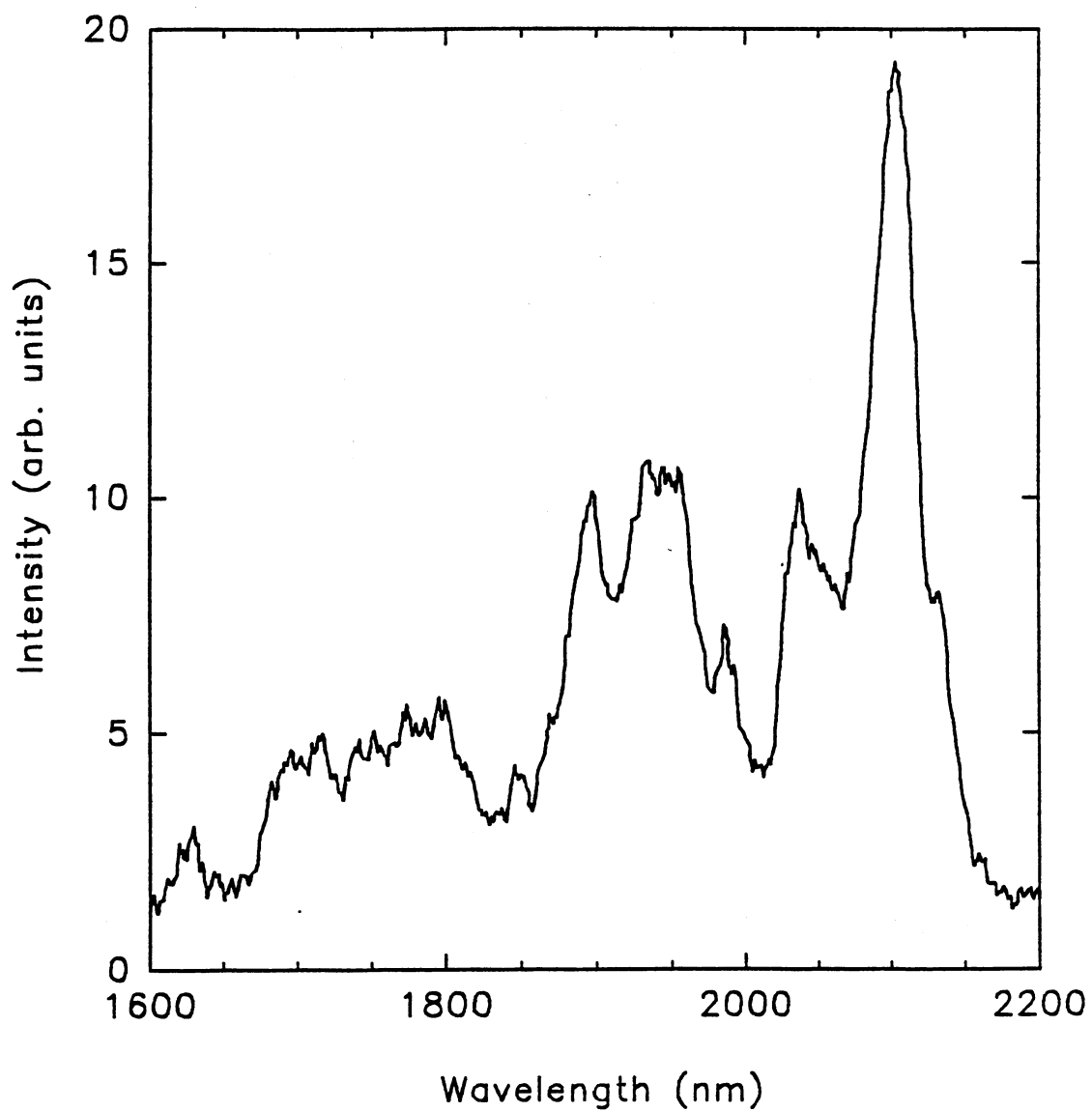


Figure 8. Fluorescence from the Tm 3F_4 level and the Ho 5I_7 level in Tm,Ho:YAG at room temperature

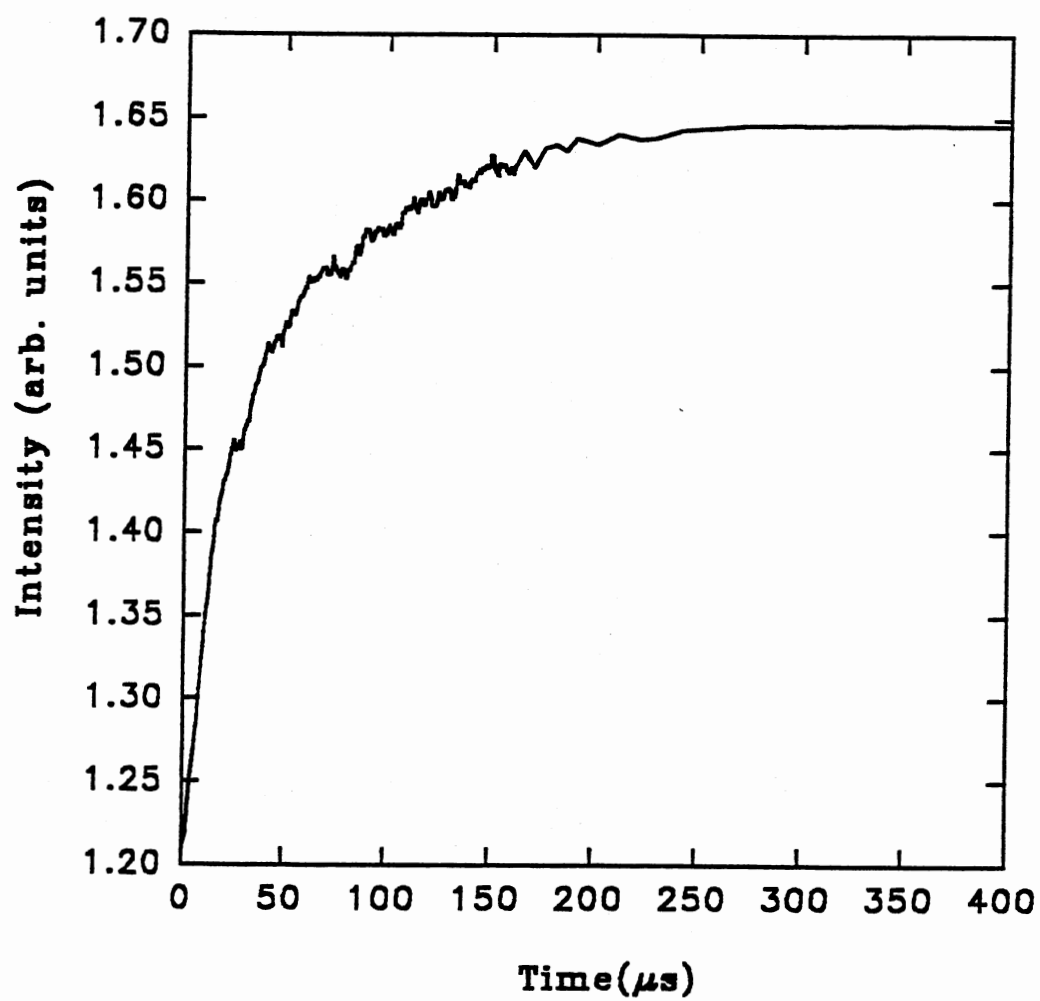


Figure 9. Rise of the fluorescence emission from the Ho 5I_7 level in Tm,Ho:YAG at room temperature after pumping the Tm ions

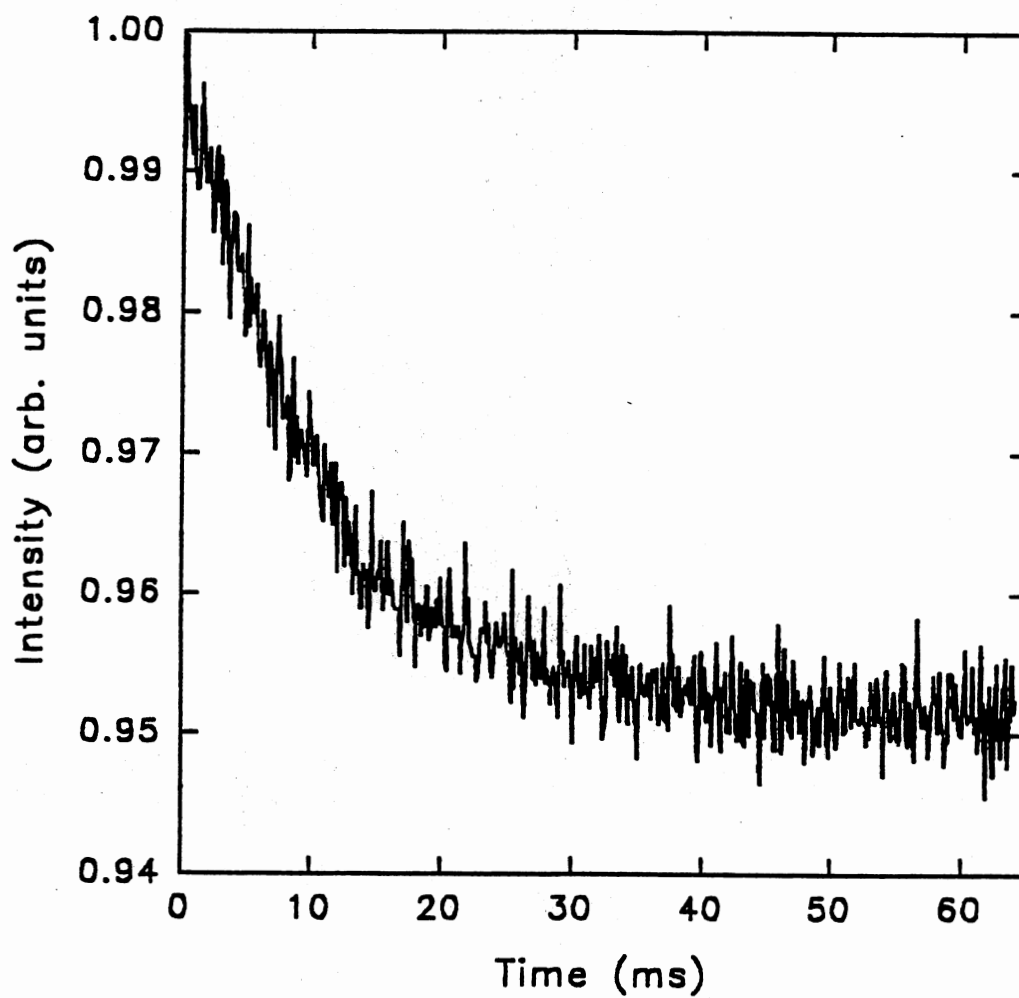


Figure 10. Fluorescence emission decay pattern from the Tm 3F_4 level in sample 4 at room temperature

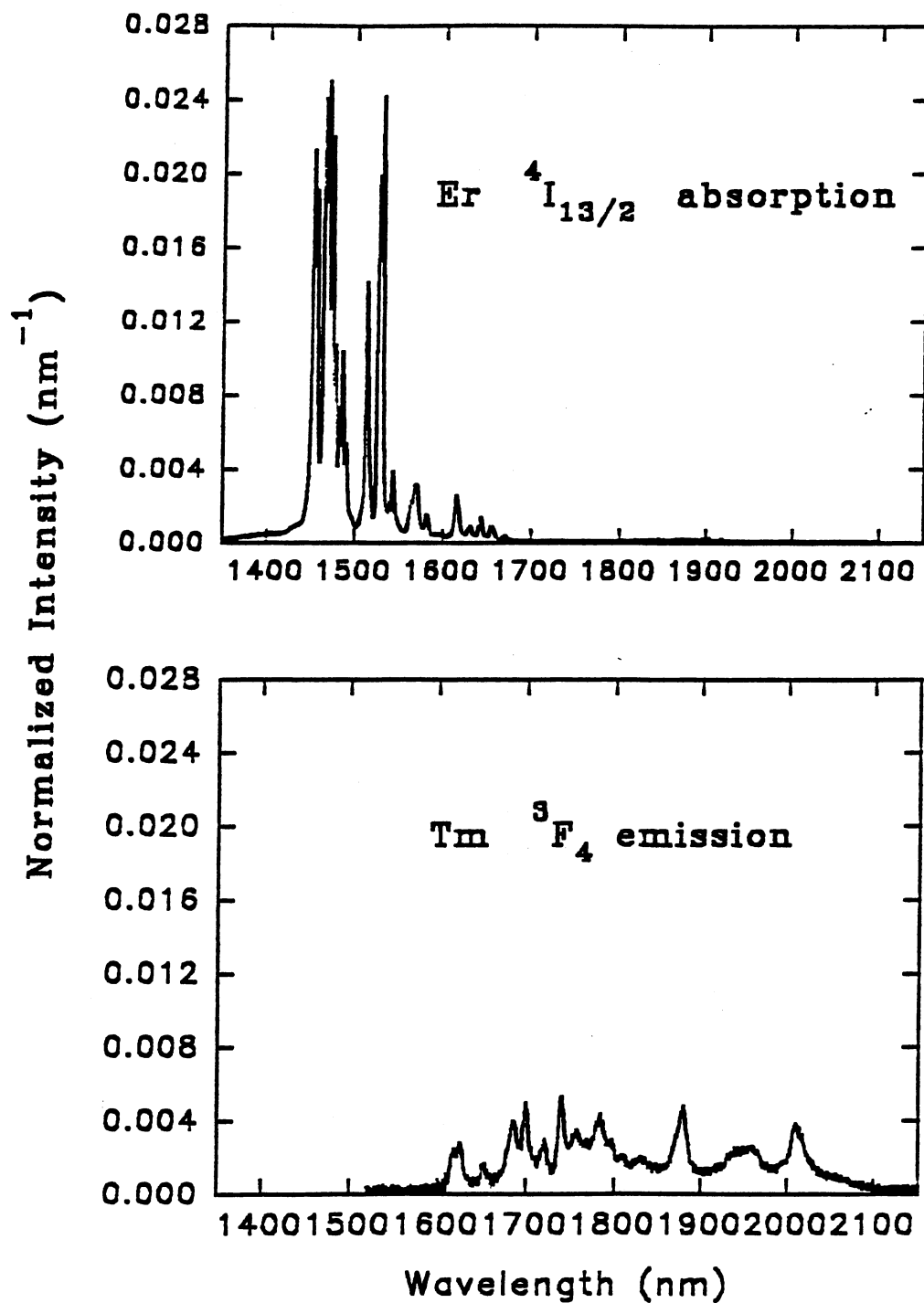


Figure 11. Normalized emission and absorption spectra of the transitions involving the Tm 3F_4 and Er $^4I_{13/2}$ energy levels, respectively, at room temperature

TABLE II
CRITICAL INTERACTION DISTANCES
CALCULATED IN THIS WORK

| Energy Transfer Process | $R_{crit.}$ | Temperature |
|------------------------------|-------------|-------------|
| | (A) | (K) |
| Tm 3F_4 - Tm 3F_4 | 16.0 | 293 |
| Tm 3F_4 - Tm 3F_4 | 11.5 | 12 |
| Tm 3F_4 - Ho 5I_7 | 17.3 | 293 |
| Tm 3F_4 - Er $^4I_{13/2}$ | 9.0 | 293 |

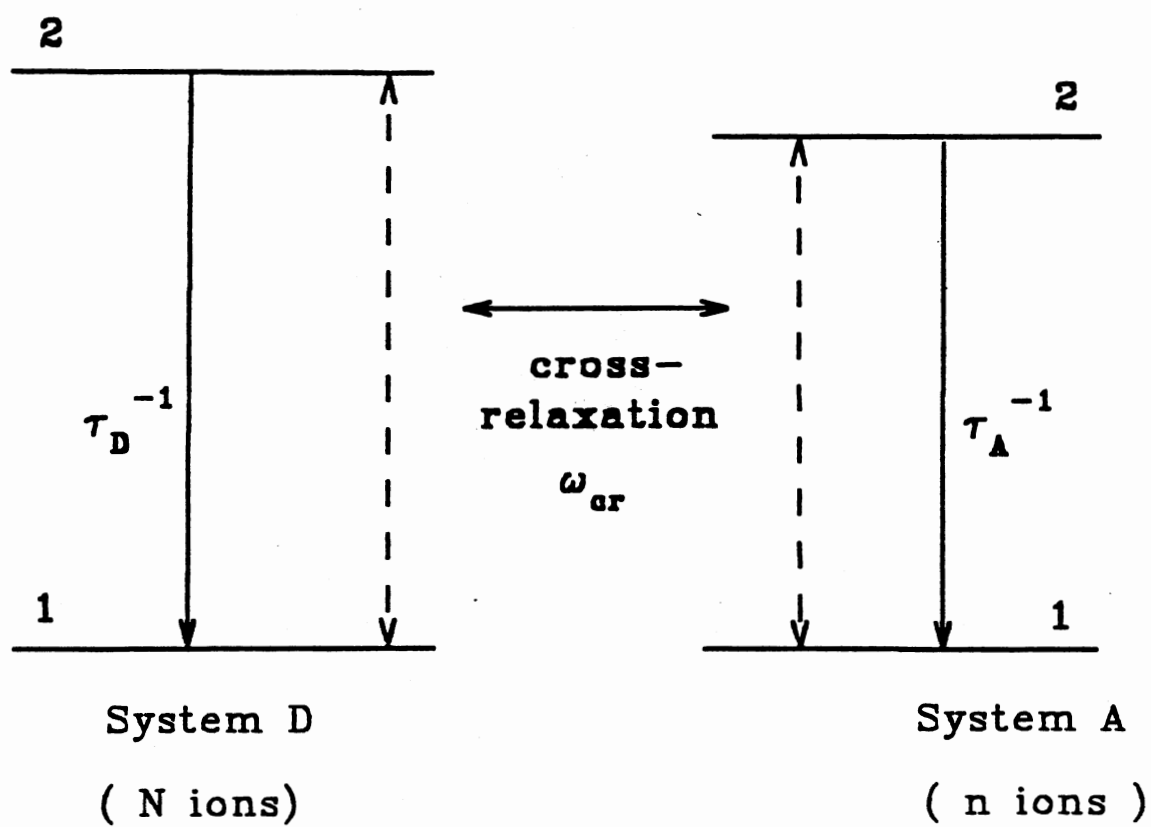


Figure 12. Nonradiative cross-relaxation between two systems of ions, D and A

various levels can be written as [14]

$$\begin{aligned}
 \frac{d}{dt}N_2 &= -\frac{1}{\tau_D}N_2 - N_2n_1\omega_{cr}/n \\
 \frac{d}{dt}N_1 &= -\frac{d}{dt}N_2 \\
 \frac{d}{dt}n_2 &= -\frac{1}{\tau_A}n_2 + N_2n_1\omega_{cr}/n \\
 \frac{d}{dt}n_1 &= -\frac{d}{dt}n_2.
 \end{aligned} \tag{64}$$

Here τ_D^{-1} is the intrinsic decay rate of the donors, D, τ_A^{-1} is the intrinsic decay rate of the acceptors, A, ω_{cr} is the cross-relaxation rate between the two systems of ions, N_1 and N_2 are the number of ions in level 1 and 2, respectively, of system D, n_1 and n_2 are the number of ions in level 1 and 2 of system A, N is the total number of ions in system D and n , the total number of ions in system A. In the above equations it is assumed that system A is pumped only through cross-relaxation from system D and that, for simplicity, there is no back-transfer from A→D. Taking the time at the end of the excitation pulse to be $t=0$, and using the approximations $N_1 \approx N$ and $n_1 \approx n$, the following solutions are obtained [14]

$$\begin{aligned}
 N_2(t) &= N_2(0) e^{-(\omega_{cr} + \tau_D^{-1})t} \\
 n_2(t) &= \left[n_2(0) + \frac{\omega_{cr}}{\omega_{cr} + \tau_D^{-1} - \tau_A^{-1}} N_2(0) \right] e^{-\frac{t}{\tau_A}} - \frac{\omega_{cr}}{\omega_{cr} + \tau_D^{-1} - \tau_A^{-1}} N_2(0) e^{-(\omega_{cr} + \tau_D^{-1})t}.
 \end{aligned} \tag{65}$$

If the excitation pulse is short enough, a maximum can occur for $n_2(t)$ at a time t_{\max} after the end of the pulse. The time t_{\max} can be calculated by setting

$$\frac{d}{dt}n_2(t_{\max}) = 0. \tag{66}$$

Using Eqs. 65 and 66 we get [14]

$$t_{\max} = \frac{1}{\tau_A^{-1} - \tau_D^{-1} - \omega_{cr}} \left\{ \ln \left[\frac{\tau_A^{-1}}{\tau_D^{-1} + \omega_{cr}} \right] + \frac{\tau_A^{-1} (\tau_D^{-1} + \omega_{cr} - \tau_A^{-1})}{(\tau_D^{-1} + \omega_{cr}) \omega_{cr}} \frac{n_2(0)}{N_2(0)} \right\}. \tag{67}$$

Eq. 67 can be applied to the Tm,Ho:YAG system, where the Tm ions are the donors, D, and the Ho ions are the acceptors, A. The fluorescence emission signal from the 5I_7 level of the Ho ions, shown in Figure 9, rises from zero to a maximum value in $330 \pm 30 \mu s$. Using this value for t_{\max} , a value of 6.5 ms for the intrinsic lifetime of the 5I_7 energy level of Ho ions in YAG [15], Eq. 67 predicts a value for the Tm→Ho energy transfer rate of $\omega_{cr} = 1.3 \times 10^4 \text{ sec}^{-1}$.

Energy transfer theories, presented earlier in this chapter, that account specifically for both energy migration among donors and transfer to acceptors were employed to calculate theoretical predictions for the overall Tm-Ho transfer rate using the data in Table II. Huber's theory (Eq.58) gives a transfer rate of $4.5 \times 10^3 \text{ sec}^{-1}$, while Blumen and Silbey's model (Eq. 63) predicts a rate of $6.3 \times 10^3 \text{ sec}^{-1}$. As can be seen from Table II, in our case $R_{0_{DD}} \approx R_{0_{DA}}$ and, in applying Burshtein theory, it is not clear whether Eq. 41 or Eq. 42 should be used, so both equations were used. The transfer rate calculated using Eq. 41 is $2.2 \times 10^3 \text{ sec}^{-1}$, while Eq. 42 gives a rate of $3.1 \times 10^3 \text{ sec}^{-1}$. It is seen that these theories predict transfer rates which are a few times lower than the value obtained from experimental data using Eq. 67. However, considering the approximations used in the theoretical models and those made in deriving Eq. 67, the results presented above are in reasonably good agreement.

Fluorescence spectroscopy investigations performed at room temperature on sample no.7 by pumping directly the 1G_4 level of the Tm ions showed that no fluorescence emission from the Er ions occurred. This implies that, under these excitation conditions, no detectable energy transfer from the Tm to the Er ions takes place. This result is not surprising, considering that the critical interaction distance calculated for the Tm-Er energy transfer is much smaller than the value obtained for the efficient Tm-Ho transfer process which has been observed experimentally.

Transient Laser-Induced Grating Spectroscopy

Laser-induced grating (LIG) spectroscopy has been shown to be an important method of investigating energy transfer among ions in solids [26-28]. It is the only experimental technique that can directly measure resonant interactions that result in spatial energy migration without spectral transfer.

In this research LIG spectroscopy measurements were performed using non-degenerate four-wave-mixing techniques to write and probe transient population gratings of Tm^{3+} ions in the 3F_4 energy level. In order to use LIG spectroscopy to

study the excitation migration among the Tm^{3+} ions in the $^3\text{F}_4$ metastable state, the LIG decay dynamics were measured for different grating spacings. As the grating spacing decreases, energy migration from the peak to the valley regions of the grating becomes more efficient in destroying the LIG.

LIG spectroscopy is capable of detecting energy migration processes only when the migration occurs over a distance comparable with the size of the peak-to-valley region of the grating; it is not capable of detecting short-range energy transfer processes.

Theoretical Background

The excitation migrating on a lattice of donors can be considered to be a localized exciton, sometimes referred to as a Frenkel or Davydov exciton [8]. The dynamics of exciton motion can be described by the Generalized Master Equation (GME) approach [29–33], which provides a unified analysis of coherent and incoherent excitation migration processes among donor ions in crystals. The GME is given by [29]

$$\frac{dP_m(t)}{dt} = \int_0^t dt' \sum_n [W_{mn}(t-t') P_n(t') - W_{nm}(t-t') P_m(t')] - \frac{P_m(t)}{\tau} \quad (68)$$

Here τ is the exciton lifetime, $P_n(t)$ is the probability of occupation of site n , and $W_{mn}(t)$ is the rate of energy transfer from site m to site n ; it is called the "memory function" and describes the degree of coherence of the exciton migration process [29]. The fundamental problem of the GME theory is the calculation of the memory functions. Consider an exciton in a crystal of N sites with all site energies equal and site-to-site interaction matrix elements V_{mn} ($V_{mn} = \langle m | H | n \rangle$). In the absence of phonons the exciton motion is purely coherent and is governed by the Schroedinger equation [30]

$$\frac{dc_m}{dt} = -i \sum_n V_{mn} c_n. \quad (69)$$

Here $c_m(t) = \langle m | \psi(t) \rangle$ is the amplitude at the m^{th} site, $|m\rangle$ is a localized state, $|\psi\rangle$ is the system state, \hbar is taken to be equal to 1, and

$$c_m^* c_m = P_m. \quad (70)$$

To calculate the memory functions, Equation 68 can be rewritten as [29]

$$\frac{dP_m(t)}{dt} + \int_0^t dt' \sum_n A_{mn}(t-t') P_n(t') = 0 \quad (71)$$

where

$$A_{mm} = \sum_n W_{nm} \quad (72)$$

and

$$A_{mn} = -W_{mn} \quad (73)$$

for $m \neq n$, and the exciton lifetime is neglected for the time being. Due to the translational invariance of the system, we can write $A_{mn} = A_{m-n,0} = A_{m-n}$. Introducing the discrete Fourier transforms of $P_m(t)$ and $A_{m-n}(t)$

$$P^k(t) = \sum_m P_m(t) e^{ikm} \quad (74)$$

$$A^k(t) = \sum_l A_l(t) e^{ikl} \quad (75)$$

and taking the Fourier and Laplace transforms of Equation 71 leads to a solution for the memory functions [29] in the form

$$\tilde{A}^k(\epsilon) = \left[\frac{1}{\tilde{P}^k(\epsilon)} \right] - \epsilon. \quad (76)$$

Here ϵ is the Laplace variable and tildes denote Laplace transforms. In obtaining Equation 76 the initial condition that the exciton occupies a single site, labelled zero, was used (i.e. $P_0(0) = 1$). The probabilities $P_m(t)$ can be calculated from Equation 69 through the discrete Fourier transform technique and by using Equation 70. The result is [29]

$$P_m(t) = \frac{1}{N} \sum_{k,q} e^{-it(V^k - V^q)} e^{-im(k-q)} \quad (77)$$

where V^k is the discrete Fourier transform of V_{m-n} defined as in Equation 75. Using Equations 77 and 74 in Equation 76, the memory functions for coherent exciton motion can be calculated [29] as

$$W_{mn}(t) = - \int d\epsilon e^{\epsilon t} \sum_k \left\{ \frac{e^{-ik(m-n)}}{\sum_q [\epsilon + i(V^{k+q} - V^q)]^{-1}} \right\}. \quad (78)$$

Here the ϵ integration is on the Bromwich contour and constitutes the Laplace inversion. It should be pointed out that Equation 78 is valid for any form and strength of the intersite interaction, V_{mn} , any lattice type and any size of the crystal, provided that translational invariance applies. The case of partially coherent motion in which the exciton interacts with the phonon bath is treated by introducing the phonon scattering rate, α . The memory functions in this case are obtained [30] from Equation 78 by replacing ϵ with $(\epsilon + \alpha)$.

The infinite one-dimensional crystal with nearest-neighbor interactions given by

$$V_{mn} = V(\delta_{m,n+1} + \delta_{m,n-1}) \quad (79)$$

provides a particular case of interest because it approximates the one-dimensional nature of the transient excited state population gratings. The Fourier transform of Equation 79 gives

$$V^k = 2V \cos k \quad (80)$$

and the double transform $\widetilde{W}^k(\epsilon)$ of the memory functions can be evaluated exactly [29] as

$$\widetilde{W}^k(\epsilon) = - \left[\epsilon^2 + 16V^2 \sin^2 \left(\frac{k}{2} \right) \right]^{1/2}. \quad (81)$$

Using Equations 72 and 73 we have [29]

$$\widetilde{A}^k(\epsilon) = \widetilde{W}^0(\epsilon) - \widetilde{W}^k(\epsilon) \quad (82)$$

and recognizing the Laplace transform of $(1/t) J_1(t)$ or of $[J_0(t) + J_2(t)]$, we can write [30]

$$A^k(t) = \left[8V^2 \sin^2(k/2) \right] \{ J_0[4Vt \sin(k/2)] + J_2[4Vt \sin(k/2)] \} \quad (83)$$

where J_0 and J_2 are the Bessel functions. Taking the inverse Fourier transform of Equation 83 and using Bessel function identities, the memory functions $W_{mn}(t)$ can be calculated as [30]

$$\begin{aligned} W_{mn}(t) = 2V^2 [& J_{m-n+1}^2(2Vt) + J_{m-n-1}^2(2Vt) + \\ & 2J_{m-n-1}(2Vt)J_{m-n+1}(2Vt) - 2J_{m-n}^2(2Vt) - \\ & J_{m-n}(2Vt)J_{m-n+2}(2Vt) - J_{m-n}(2Vt)J_{m-n-2}(2Vt)]. \end{aligned} \quad (84)$$

Here $J_i(2Vt)$ is the Bessel function of order i . Equation 84 can also be written in the compact form [29]

$$W_{mn}(t) = \frac{1}{t} \frac{d}{dt} J_{m-n}^2(2Vt) \quad (85)$$

Equation 84 shows that memories exist between every pair of sites in the crystal although the Hamiltonian has only nearest-neighbor matrix elements. The memory functions for partially coherent exciton motion are obtained [29] by multiplying the right-hand side of Equation 84 by $e^{-\alpha t}$, i.e.

$$\begin{aligned} W_{mn}(t) = 2V^2 e^{-\alpha t} \{ & J_{m-n+1}^2(2Vt) + J_{m-n-1}^2(2Vt) + \\ & 2J_{m-n-1}(2Vt)J_{m-n+1}(2Vt) - 2J_{m-n}^2(2Vt) - \\ & J_{m-n}(2Vt)[J_{m-n+2}(2Vt) + J_{m-n-2}(2Vt)] \}. \end{aligned} \quad (86)$$

Equation 86 is valid for any degree of coherence. The incoherent limit is obtained from this equation when $\alpha \rightarrow \infty$, $V \rightarrow \infty$, such that $V^2/\alpha = \text{const.}$ In this case, the GME with the memory functions 86 reduces to the Master Equation [29]

$$\frac{dP_m(t)}{dt} = F [P_{m+1}(t) + P_{m-1}(t) - 2P_m(t)] \quad (87)$$

where $F = 2V^2/\alpha$ is the nearest-neighbor transfer rate.

The GME formalism can be applied to the analysis of transient grating experiments by noticing that the square root of the grating signal intensity is essentially the Fourier component $P^\eta(t)$ of the probabilities $P_m(t)$ [29]

$$[I(t)]^{1/2} = \text{const.} \sum_m P_m(t) e^{i\eta m} = \text{const.} P^\eta(t) \quad (88)$$

where η is the dimensionless wavevector of the transient grating

$$\eta = \left(\frac{4\pi a}{\lambda} \right) \sin(\theta/2). \quad (89)$$

Here a is the intersite separation, λ is the excitation wavelength and θ is the crossing angle of the exciting beams that write the grating. The theoretical problem is therefore the one of calculating the solutions of the GME 68 in the Fourier domain with the initial condition [29]

$$P_m(0) = \text{const.} [1 + \cos(\eta m)] \quad (90)$$

which corresponds to only three Fourier components P^0 , P^η , $P^{-\eta}$ being excited. Equations 68, 71 and 90 lead to [29]

$$\frac{dS(t)}{dt} + \frac{S(t)}{\tau} + \int_0^t dt' A^\eta(t-t') S(t') = 0 \quad (91)$$

where

$$S(t) = [I(t)]^{1/2}, \quad (92)$$

τ is the exciton lifetime and $A^\eta(t)$ is the Fourier transform of $A_{m-n}(t)$. Taking the Laplace transform of Equation 91 gives [29]

$$\tilde{S}(\epsilon) = S(0) \left[\epsilon + \frac{1}{\tau} + \tilde{A}(\epsilon) \right]^{-1}. \quad (93)$$

Taking the inverse Laplace transform of Equation 93 and using Equations 81, 82 and 92 gives [31]

$$I(t) = I(0) e^{-\frac{2t}{\tau}} \left(\int d\epsilon e^{\epsilon t} \left\{ \left[\epsilon^2 + 16V^2 \sin^2 \left(\frac{\eta}{2} \right) \right]^{1/2} - \alpha \right\}^{-1} \right)^2 \quad (94)$$

where the ϵ integration is on the Bromwich contour. An explicit evaluation of the Laplace transform in Equation 94 leads to [31]

$$I(t) = I(0) e^{-\frac{2t}{\tau}} \left[1 - e^{-\alpha t} b \int_0^t du J_1(bu) e^{\alpha(t^2-u^2)^{1/2}} \right]^2 \quad (95)$$

where

$$b = 4V \sin(\eta/2). \quad (96)$$

Equation 95 can be rewritten by integrating by parts, using recurrence formulas for Bessel functions and making a change of variables. The result is [32,33]

$$I(t) = I(0) e^{-\frac{2t}{\tau}} \left\{ J_0(bt) e^{-\alpha t} + \alpha \int_0^t du J_0 \left[b(t^2 - u^2)^{1/2} \right] e^{-\alpha(t-u)^2} \right\}^2. \quad (97)$$

Equation 97 gives the transient grating intensity for any degree of coherence of the exciton migration process. The extreme limits are obtained immediately. For purely coherent motion, $\alpha = 0$ and we get an oscillatory signal [31]

$$I(t) = I(0) e^{-\frac{2t}{\tau}} [J_0(bt)]^2. \quad (98)$$

For completely incoherent motion with small intersite interactions, $\alpha \rightarrow \infty$, $V \rightarrow \infty$, $2V^2/\alpha = F$, and we get, from Equation 94, a purely exponential signal [31]

$$I(t) = I(0) e^{-\frac{2t}{\tau}} \exp \left\{ -2t \left[4F \sin^2(\eta/2) \right] \right\}. \quad (99)$$

For incoherent exciton motion with arbitrary value of the ratio V/α , the transient grating signal intensity is given by [31,32]

$$I(t) = I(0) \exp \left\{ -2t \left[\left(\alpha + \frac{1}{\tau} \right)^2 + 16V^2 \sin^2(\eta/2) \right]^{1/2} - \alpha \right\}. \quad (100)$$

This equation is significant because of its ability to describe any degree of coherence present in signals which appear to be exponential. This is particularly important when the time resolution of the experiment is much coarser than $1/\alpha$ and the rich structure given by Equation 97 is entirely hidden.

In the continuum limit (i.e. the crystal is approximated by a continuum), $a \rightarrow 0$ which implies $\eta \rightarrow 0$ and Equation 99 gives in this case [31]

$$I(t) = I(0) e^{-\frac{2t}{\tau}} \exp \left[-2t \Delta^2 D \right] \quad (101)$$

where $\Delta = \eta/a$ and $D = Fa^2$ is the exciton diffusion constant. Equation 101 represents the result obtained by Salcedo et al. [26]. Their theoretical approach assumed that the exciton population distribution, $n(x,t)$, evolves in time through the continuum diffusion equation

$$\frac{\partial n(x,t)}{\partial t} = D \frac{\partial^2 n(x,t)}{\partial x^2} - \frac{\partial n(x,t)}{\tau} \quad (102)$$

with the initial condition

$$n(x,0) = \frac{1}{2} [1 + \cos(\Delta x)] \quad (103)$$

Equations 102 and 103 lead to the solution [26]

$$n(x, t) = \frac{1}{2} e^{-\frac{t}{\tau}} \left[1 + e^{-\Delta^2 D t} \cos(\Delta x) \right]. \quad (104)$$

The transient signal is proportional to the square of the grating depth, i.e.

$$I(t) \propto \left[n(0, t) - n\left(\frac{\Lambda}{2}, t\right) \right]^2 \quad (105)$$

where

$$\Lambda = \lambda / [2 \sin(\theta/2)] \quad (106)$$

is the grating spacing. Equations 104 and 105 lead to the result given by Equation 101.

The ion-ion interaction rate, V , and the exciton scattering rate, α , can be used to calculate the parameters describing the exciton migration properties. These parameters are the diffusion coefficient

$$D = 2V^2 a^2 / \alpha, \quad (107)$$

the mean free path

$$L_m = (2)^{1/2} V a / \alpha, \quad (108)$$

the diffusion length

$$L_D = (2D\tau)^{1/2} \quad (109)$$

and the number of sites visited between scattering events

$$N_s = L_m / a. \quad (110)$$

Experimental Procedure

The experimental setup for nondegenerate four-wave-mixing (FWM) is shown in Figure 13. The output of an argon-ion laser tuned to the 465.8 nm emission line was used to excite resonantly the 1G_4 level of the Tm ions. The laser output with a power of 85 mW was split into two beams (write beams) of equal intensity, which were focused to waists of $\sim 300\mu\text{m}$ and crossed inside the sample at an angle θ to

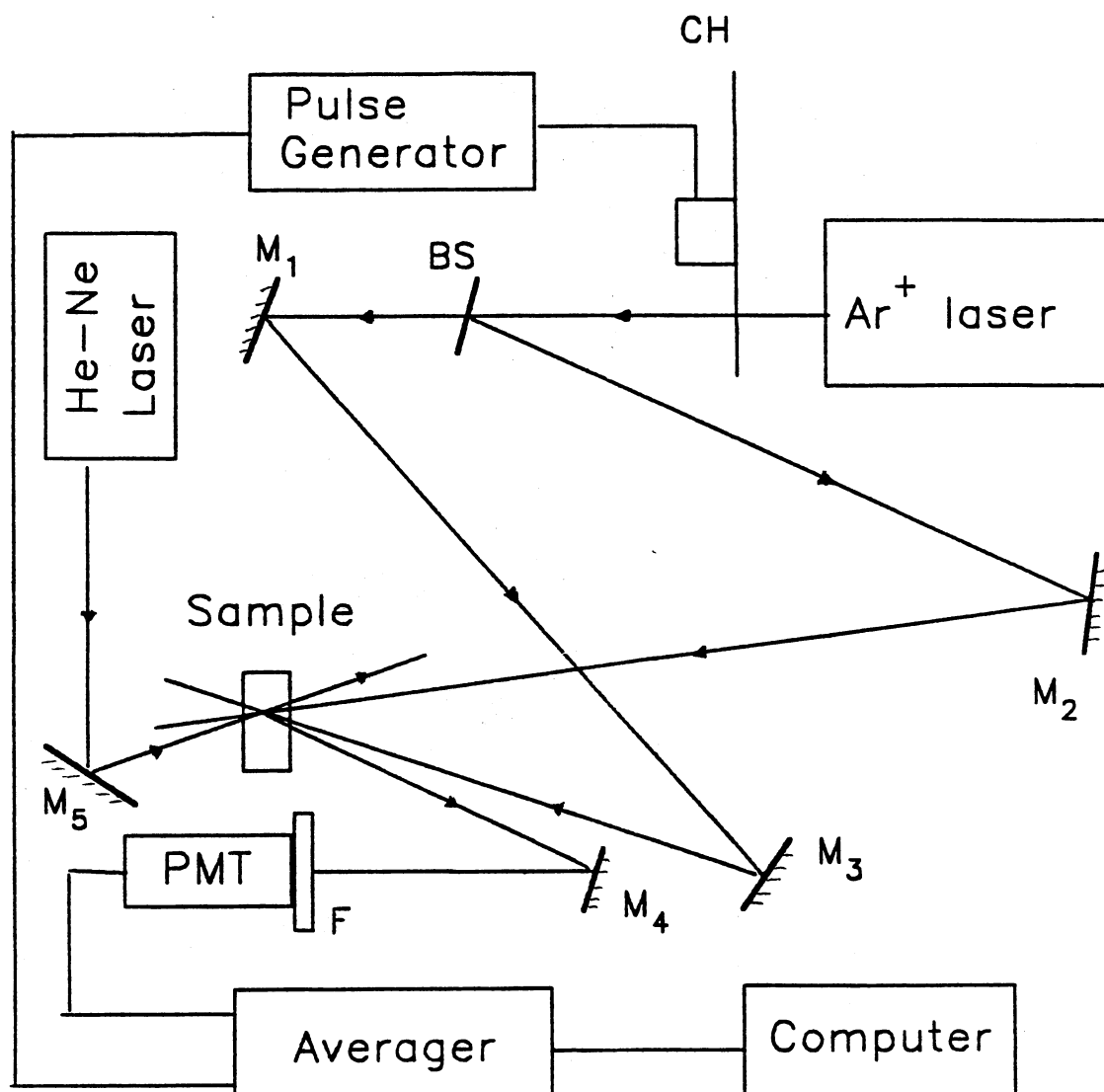


Figure 13. Experimental setup for nondegenerate four-wave-mixing; M-mirrors; BS-beam splitter; CH-chopper; F-filter; PMT-photomultiplier tube

form a sine wave interference pattern. The difference in the optical path lengths of the write beams was less than the coherence length of the laser. Through optical absorption the sinusoidal interference pattern of the write beams created a spatial population distribution of the Tm ions in the 3F_4 metastable state with the same pattern. Owing to the difference in the complex refractive index between the regions of high concentration of ions in the excited state and those containing ions in the ground state, this population distribution acted as a refractive-index grating. To probe the properties of this LIG, the output of a 15 mW He-Ne laser at 632.8 nm was used. The probe beam was focused on the grating with a beam waist of $\sim 200\mu\text{m}$. Its alignment was carefully adjusted to satisfy the Bragg scattering condition for the orientation of the LIG. The scattered signal beam was detected by an RCA C31034 photomultiplier tube with a He-Ne laser-line interference filter, used to eliminate the sample fluorescence, and was then processed by an EG&G signal averager and stored on a computer. To analyse the transient behavior of the grating, the write beams were mechanically chopped off and on. For the low temperature measurements a cryostat with a closed cycle helium refrigerator and a Lake Shore temperature controller were used.

Experimental Results and Interpretation

The laser write beams resonantly excite the 1G_4 level of the Tm ions after which there is rapid radiative and non-radiative relaxation to the 3F_4 level. After relaxation to the 3F_4 level, long range energy migration occurs. This process was investigated using LIG spectroscopy. Laser-induced grating decay kinetics were measured in samples 1, 2 and 3 for different grating spacings and different temperatures. No LIG signal was detected in sample 4 for write beams crossing angles greater than 3° , probably due to the very low concentration of Tm ions in this sample. The decay kinetics were found to be exponential, and consistent with the fluorescence decay dynamics of the Tm 3F_4 metastable level in each of the samples investigated. This shows that for these excitation conditions the LIG

signals are associated with transient population gratings of Tm^{3+} ions in this metastable level. The LIG signal transient decays were found to be dependent on the grating spacing in all three samples, indicating the presence of long range energy migration. This dependence weakens considerably at low temperatures, implying lower migration rates at these temperatures. Figure 14 shows a typical LIG transient decay curve at room temperature and a grating spacing of $3.3 \mu\text{m}$ (i.e. a crossing angle between the write beams of 8°). The filled circles represent experimental points, and the solid line is the theoretical prediction discussed below.

The properties of the LIG transient decay kinetics provide information about the excitation migration among Tm ions in the metastable state. To model the LIG decay dynamics, the generalized master equation (GME) theory developed by Kenkre was used. For transient LIG signals exhibiting exponential decays, the time dependence of the signal is given by Eq. 100. This equation was fit to the measured transient LIG signal decays, treating V and α as adjustable parameters. The distance a was taken to be the average nearest neighbor distance between Tm^{3+} ions assuming a random distribution. This is given by [34]

$$a = 0.55(n_{\text{Tm}})^{-1/3} \quad (111)$$

where n_{Tm} is the concentration of the Tm^{3+} ions in the sample. The LIG decay kinetics were investigated for several grating spacings and for a variety of temperatures and Tm^{3+} ion concentrations. Typical values of α and V obtained from fitting Eq. 100 to these data are listed in Table III, where the \pm error bars express the sensitivity of the fit to the listed values of the adjustable parameters. It should be pointed out that the fits were not unique, but other values of α and V that gave equivalent fits to the data had magnitudes that were not physically reasonable for these parameters.

A theoretical estimate for the ion-ion interaction rate can be obtained using Eq. 38. If we consider the excitation migration as a nearest-neighbor hopping process, an average ion to ion hopping time can be defined as

$$\varphi(\tau_{\text{hop}}) = e^{-1} \quad (112)$$

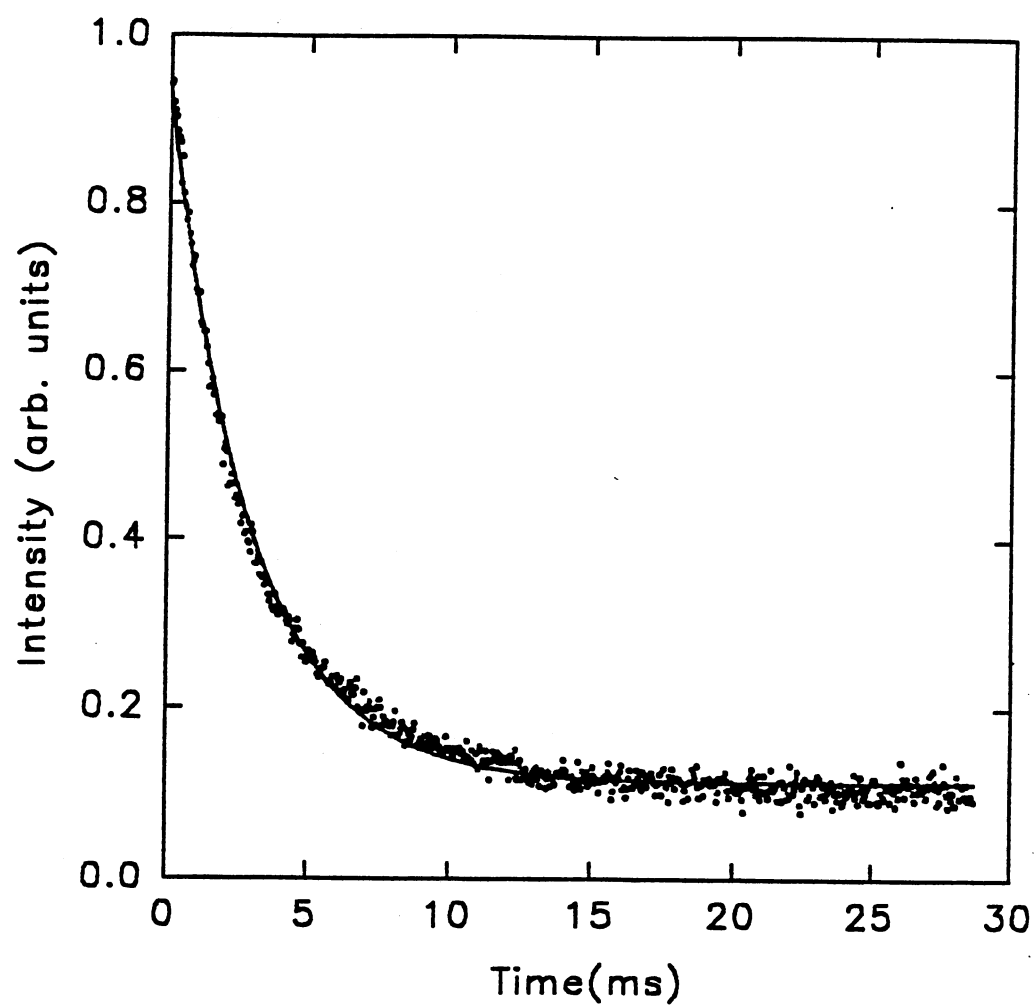


Figure 14. LIG transient decay pattern from sample 1 at room temperature and a grating spacing of $3.3 \mu\text{m}$. Filled circles - experimental points, solid line - theoretical fit

TABLE III
ION-ION INTERACTION RATE AND EXCITON
SCATTERING RATE AT ROOM
TEMPERATURE

| Sample | α | V | a |
|--------|-----------------------------|-----------------------------|----------------------------|
| No. | $\times 10^3 \text{s}^{-1}$ | $\times 10^3 \text{s}^{-1}$ | $\times 10^{-8} \text{cm}$ |
| 1 | 5.0 ± 2.0 | 170 ± 30 | 4.9 |
| 2 | 1.5 ± 0.6 | 62 ± 12 | 5.9 |
| 3 | 0.7 ± 0.3 | 27 ± 6 | 6.7 |
| 6 | 0.5 ± 0.2 | 65 ± 12 | 5.9 |

and an average ion-ion interaction rate can be calculated using Eqs. 38 and 112

$$(\tau_{hop})^{-1} = \gamma^2. \quad (113)$$

Above, γ is given by Eq. 37, where, for the case considered here, R_0 represents the critical interaction distance for the Tm-Tm migration process and c_A is the concentration of Tm ions (both the donors and acceptors are Tm ions). Figure 15 shows a plot of the nearest neighbor interaction rate, V , versus Tm concentration. The solid circles represent the values of V determined from fitting Eq. 100 to the experimental data. The line represents the theoretical prediction for the average ion-ion interaction rate calculated using Eq. 113. The value used for τ_D in Eq. 113 was 11 ms. This was obtained from the fluorescence lifetime of the Tm 3F_4 level measured in a lightly doped sample (sample 4). As can be seen in Figure 15, there is a good agreement between the values of V determined from experimental data and those predicted theoretically.

The ion-ion interaction rate and the excitation scattering rate obtained from the experimental data can be used in Eqs. 107, 108, 109 and 110 to calculate the parameters describing the exciton migration properties. The values obtained for these parameters for each of the samples investigated are listed in Table IV, where D_{exp} represents the diffusion coefficients calculated using the experimental results and Eq. 107 and D_{theory} are the theoretical predictions discussed below. Tables III and IV show that, for each sample, $\alpha < V$, and $a < L_m \ll \Lambda$ (Λ is of the order of a few microns). Thus the excitation migration in these samples is a long mean-free-path type of random walk instead of a migration in which each step of the random walk involves a scattering event.

A theoretical prediction for the diffusion coefficient for energy migration among the donors (Tm ions) can be calculated using Eq. 62. The values obtained, listed in Table IV, are of the order of 10^{-11} - 10^{-10} cm²/s, which is more than two orders of magnitude smaller than the measured values. The large discrepancy between the predicted values of D and those obtained from the experimental results may be partly due to the fact that the theoretical models presented in the

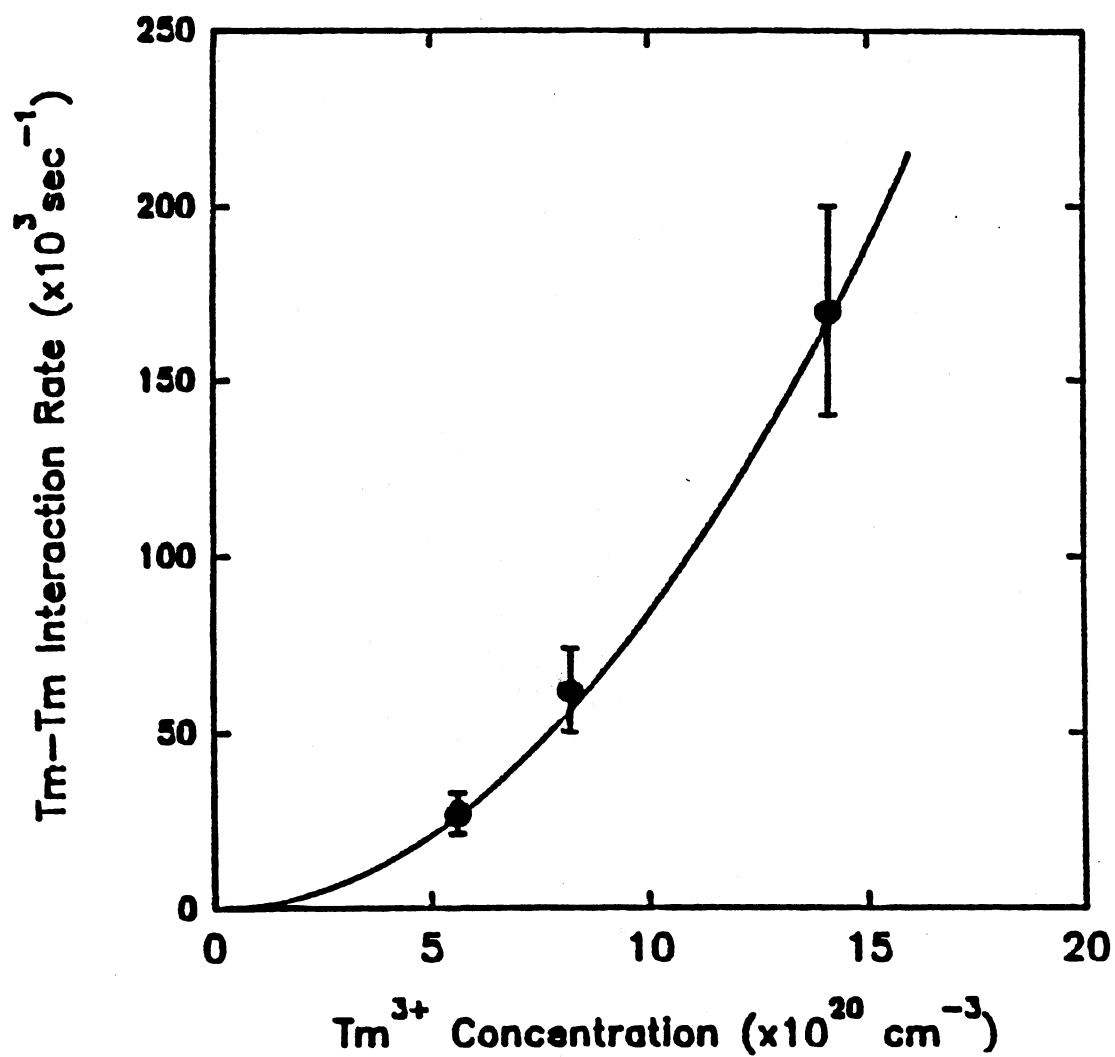


Figure 15. Variation of the ion-ion interaction rate with Tm concentration at room temperature. Filled circles - experimental points, line - theoretical prediction

TABLE IV
EXCITATION MIGRATION PARAMETERS
AT ROOM TEMPERATURE

| Sample | D_{exp} | L_m | L_D | N_S | D_{theory} |
|--------|------------------------|----------------------------|----------------------------|-------|------------------------|
| No. | cm^2/s | $\times 10^{-8} \text{cm}$ | $\times 10^{-5} \text{cm}$ | | cm^2/s |
| 1 | 3.0×10^{-8} | 240.4 | 2.19 | 48 | 1.0×10^{-10} |
| 2 | 1.8×10^{-8} | 344.9 | 1.53 | 58.5 | 0.6×10^{-10} |
| 3 | 0.9×10^{-8} | 365.5 | 1.34 | 54.5 | 0.4×10^{-10} |
| 6 | 5.9×10^{-8} | 1085 | 2.30 | 183.9 | 0.6×10^{-10} |

section "Multistep Energy Transfer" consider the excitation migration among the donor ions as a process in which a scattering event occurs on every hop of the excitation to another site. This corresponds to excitation migration parameters, $\alpha \approx V$. However, the analysis of the LIG data obtained here has shown that $\alpha \ll V$ for the samples investigated here.

The values of the excitation migration parameters for sample 2 which is co-doped with Ho ions can be used to estimate the overall energy transfer rate from the Tm to the Ho ions. Assuming a simple model of excitation hopping to the nearest neighbor (which may be either Tm³⁺ or Ho³⁺), the probability per unit time of making a hop is given by

$$P_{hop} = N_S \alpha. \quad (114)$$

Assuming the ions are uniformly distributed, the probability that a hop is to a Ho ion is 1/12 (from the ratio of the Tm and Ho ion concentrations in sample 2). The energy transfer rate from the donors (Tm ions) to the acceptors (Ho ions) can then be calculated using Eqs. 114, 110 and 108 to be

$$K_{Tm \rightarrow Ho} = (2)^{1/2} V/12. \quad (115)$$

This equation predicts an energy transfer rate of $K_{Tm \rightarrow Ho} = 7.3 \times 10^3 s^{-1}$. The value obtained here for the overall Tm-Ho transfer rate is within a factor of 2 of the value calculated in the section "Time Resolved Fluorescence Spectroscopy" using the results of the fluorescence spectral dynamics measurements. Considering the simplifying approximations used in both approaches, these values are in reasonably good agreement. One obvious simplification in the excitation hopping model is the assumption that the ions are uniformly distributed. Effects of nonuniform ion distributions and inhomogeneous broadening can affect the value derived for the overall energy transfer rate.

LIG decay kinetics were measured in sample 1 at several different temperatures. Figure 16 shows the results obtained for variation of the ion-ion interaction rate, V , with temperature. The open circles represent the values of V obtained

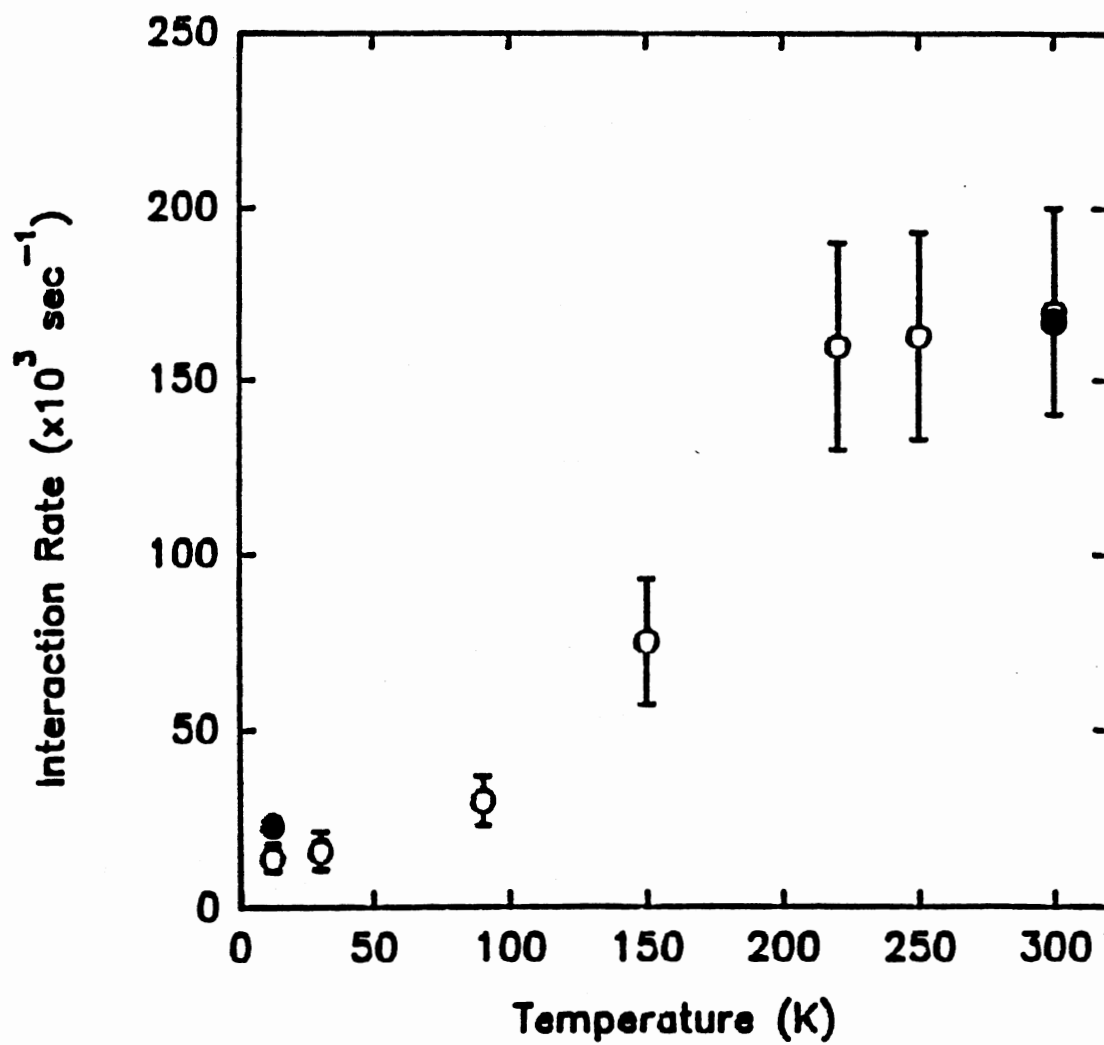


Figure 16. Variation of the ion-ion interaction rate with temperature for sample 1.
Open circles - experimental points, filled circles - theoretical values

from fitting Eq. 100 to the transient LIG signal decay curves. Using Eq. 18 and the spectra in Figure 7, the critical interaction distance at a temperature of 12 K for the Tm 3F_4 migration process was calculated to be 11.5 Å. This value was used in Eq. 113 to calculate theoretical predictions for the ion-ion interaction rate at 12 K. The filled circles represent the ion-ion interaction rates predicted by Eq. 113. As can be seen in Figure 16, the ion-ion interaction rate decreases as temperature is lowered. The good agreement between the theoretical prediction and the experimental result at 12 K, indicates that this decrease is due to the decrease in the value of the critical interaction distance due to a decrease in the spectral overlap integral as temperature is lowered.

Figure 17 shows a plot of the excitation scattering rate, α , versus temperature. The filled circles are values of α obtained from fitting Eq. 100 to the transient LIG signal decay curves. The possible excitation scattering mechanisms include scattering by defects, optical phonons, and acoustic phonons. Each of these processes has a different temperature dependence. Scattering by acoustic phonons is generally the dominant mechanism at low temperatures. This type of scattering results in a predicted temperature dependence [35] of $\alpha \propto T^{3/2}$. The solid line in Figure 17 represents a best fit to the experimental points assuming a $T^{3/2}$ dependence. As can be seen in Figure 17, this theory provides a reasonable prediction for the observed variation of α with temperature.

It is seen in Tables III and IV that the values obtained for α and D for sample no.6 differ by about a factor of 3 from the values obtained for sample no. 2, although both samples have the same Tm concentration. However, the Ho ions in sample 2 act as traps for the excitation migrating among the Tm ions, while the Er ions in sample 6 act as scattering centers and this role needs to be characterized. In order to do that, more investigations are needed to determine the type of excitation scattering mechanisms that take place in this sample.

The concentration dependence of the diffusion coefficients for energy migration in the 3F_4 level of the Tm ions determined from LIG analysis for samples 1,2 and 3 is shown in Figure 18. The circles are values calculated from experimental

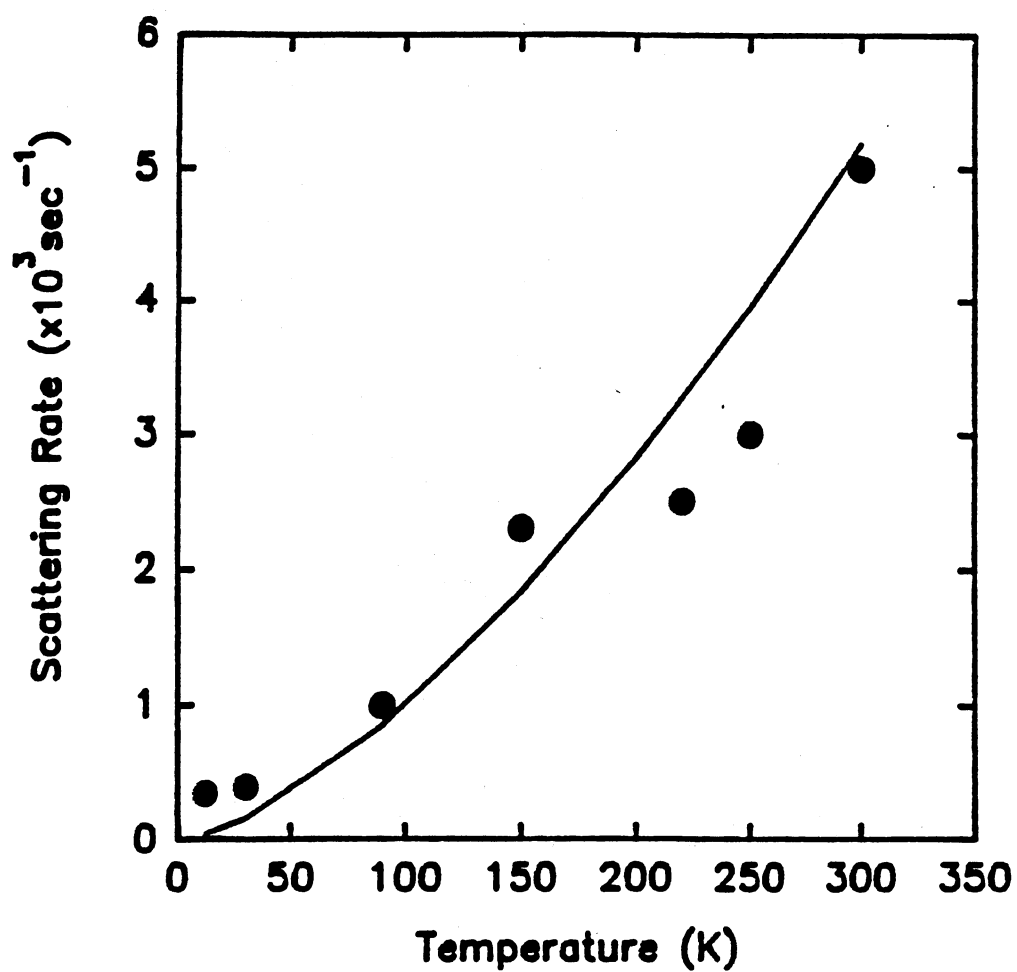


Figure 17. Variation of the excitation scattering rate with temperature for sample 1. Circles - experimental points, line - theoretical prediction

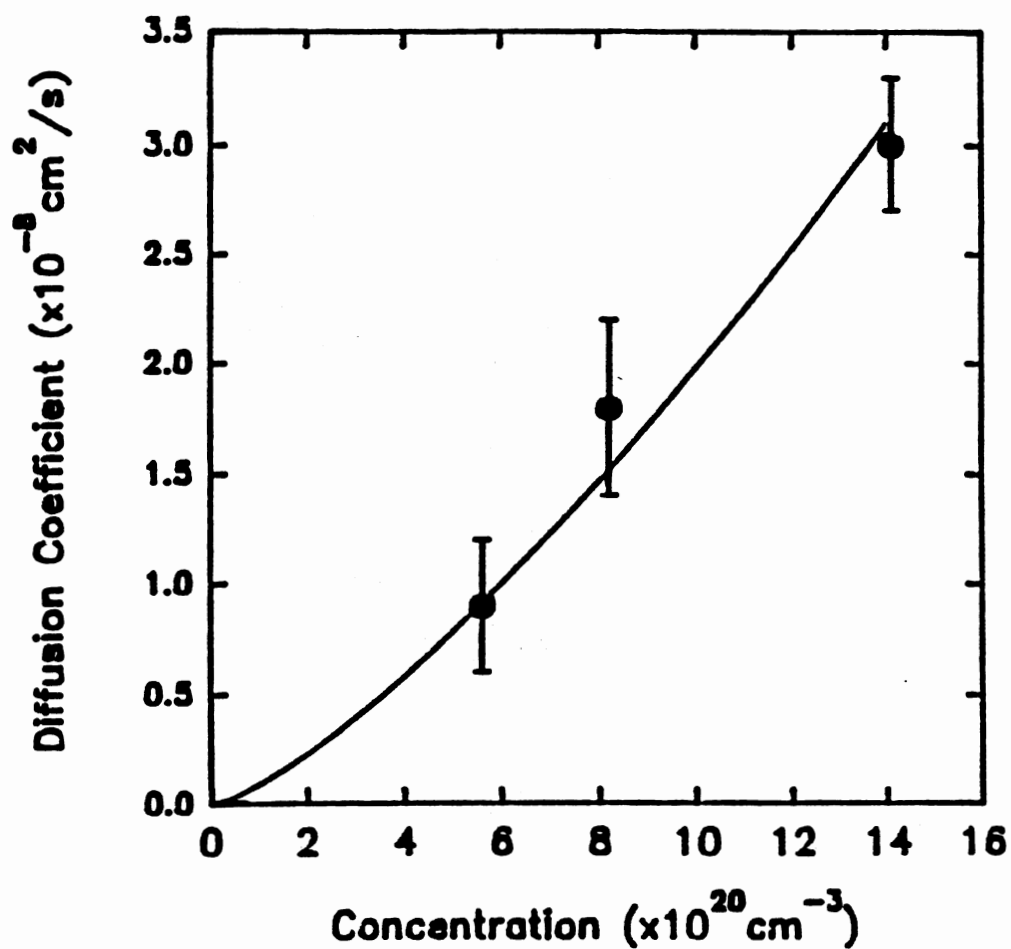


Figure 18. Variation of the diffusion coefficient with Tm concentration at room temperature. Circles - experimental points, line - theoretical prediction

results and the line represents the best fit to the experimental points assuming a $n_{Tm}^{3/4}$ dependence. As can be seen in Figure 18, this prediction is in good agreement with the observed results. This type of concentration dependence is predicted by all of the theories developed to describe a random walk type of excitation migration [16,18,23,25,29].

Discussion

Other investigations [36] have shown that there is some energy migration taking place in the Tm 3H_4 level and this enhances the cross-relaxation process that is responsible for the fluorescence quenching of this level. This migration is especially important at high levels of Tm ion concentration [36]. It should be pointed out that the excitation migration in the 3H_4 level of the Tm ions makes no discernible contribution to the measured decay characteristics of the LIG's in any of the samples investigated. This is demonstrated by the fact that the excitation lifetime in the 3H_4 level is of the order of several microseconds [36], while the excitation lifetime in the 3F_4 level and the decay times of the LIG's are on a millisecond time scale. Thus the short-lived excitation in the 3H_4 level does not migrate over long enough distances to alter the laser-induced population grating pattern.

It is known that back transfer from the 5I_7 level of the Ho ions to the 3F_4 level of Tm ions is efficient enough to lead to the condition of thermal equilibrium of the populations of these two excited states [1,3,7]. The equilibration time has been measured to be about 200 μs in a sample of similar Tm and Ho concentrations as sample no. 2 in this work [3]. Since the decay times of the LIG signals measured in this work were of the order of a few milliseconds, the presence of back transfer will simply decrease the trapping efficiency of the migrating Tm excitation energy, and not influence the dynamics of the grating decay. The efficient transfer of energy to the Ho ions can also produce a polarizability change while the ions are in the 5I_7 level. However, the intensity of LIG signal is proportional to the square of the excited state population [37]. Since the concentration of the Ho ions in

sample 2 is 12 times smaller than that of the Tm ions, the contribution of the Ho ion polarizability change to the observed LIG signal will be over two orders of magnitude smaller than the contribution to the signal made by the Tm ions. Thus this contribution will be negligible. In addition, the low concentration of Ho ions inhibits any spatial migration of energy in their 5I_7 metastable states. The ion-ion interaction rate between the Ho ions is estimated to be at least an order of magnitude smaller than that between Tm ions. Thus energy migration among the Ho ions plays no role in the LIG decay dynamics.

In sample no. 6 the excitation laser beam at 465.8 nm, which pumps the Tm 1G_4 energy level, is also absorbed into the 4T_1 band of the Cr ions. This can be seen in Figure 19 which shows the absorption spectra measured on this sample at room temperature. After exciting the Cr ions into the 4T_1 band, there is nonradiative decay to the $^4T_2/ ^2E$ states, followed by fluorescence emission from these thermally mixed levels [4]. The fluorescence emission spectra are shown in Figure 20. The fluorescence lifetime of these Cr states in the sample investigated here was measured to be $\sim 110\mu s$. Thus the excitation migration among the Cr ions in these states, if any occurs, will not influence in a discernable way the decay dynamics of the LIG's which are on a millisecond time scale. However, the Cr ions may contribute to the intensity of the observed LIG's. Since the concentration of the Cr ions is six times smaller than that of the Tm ions, the contribution of the Cr ion polarizability change to the intensity of the LIG signal will be more than 30 times smaller than the contribution made by the Tm ions.

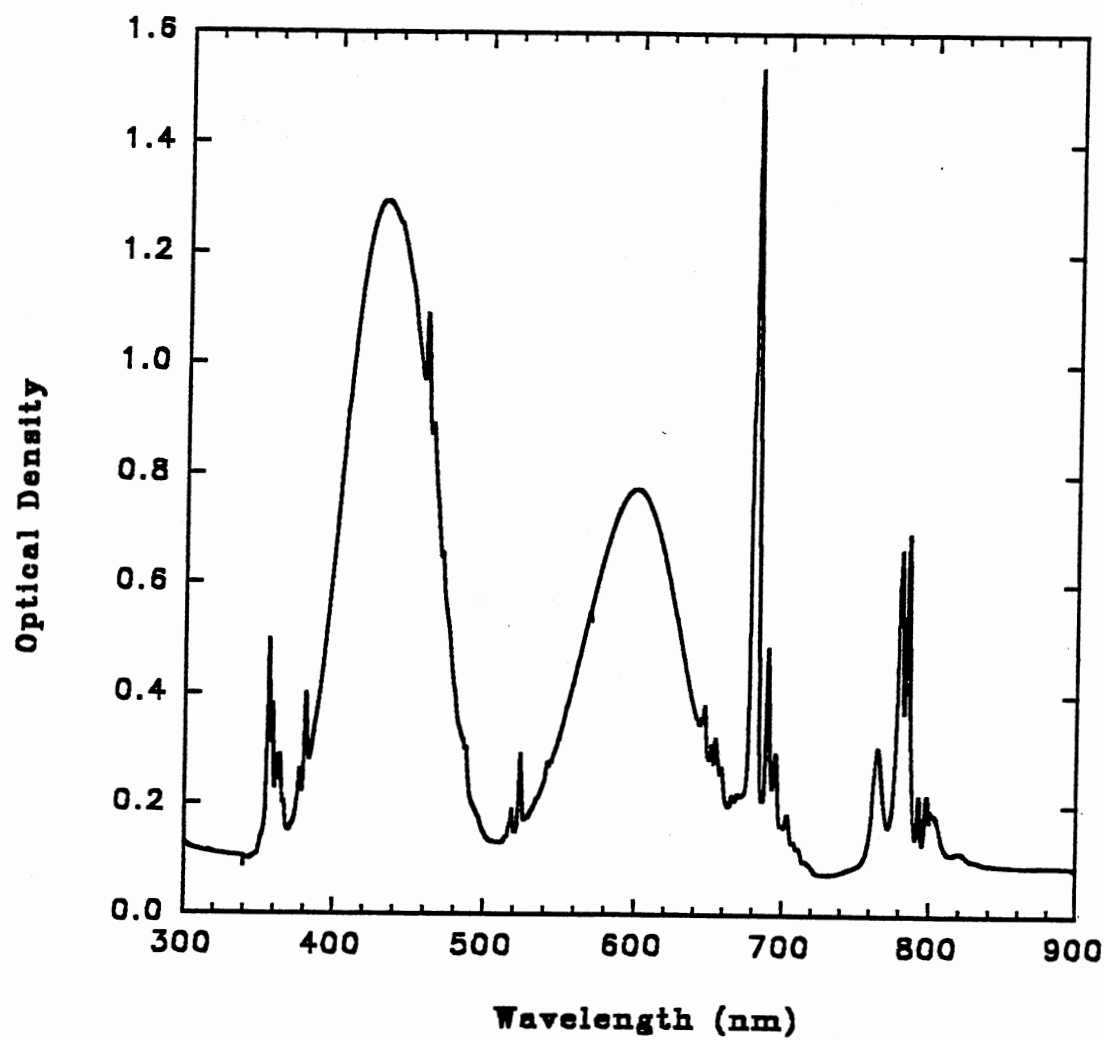


Figure 19. Absorption spectrum of Cr,Tm,Er:YAG at room temperature

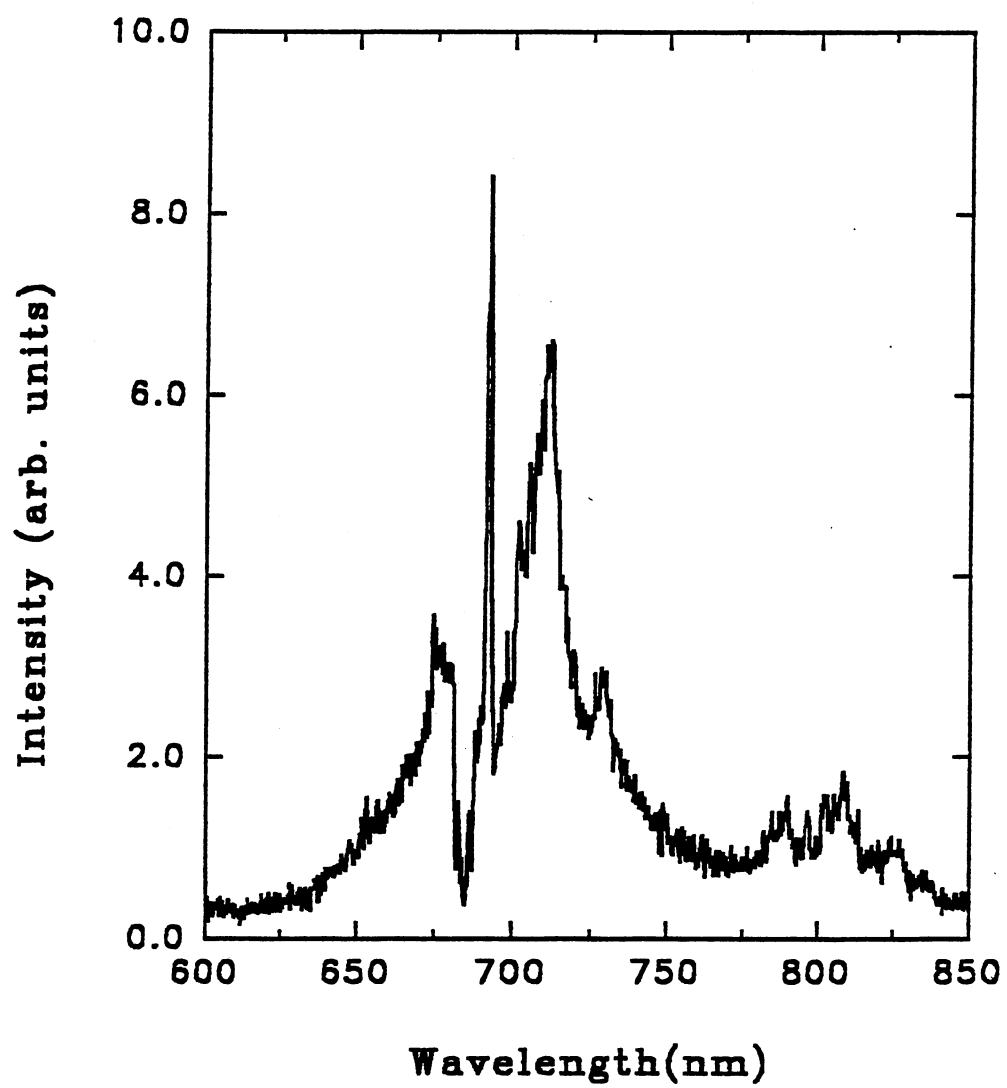


Figure 20. Fluorescence emission spectrum of Cr,Tm,Er:YAG at room temperature

CHAPTER III

REFRACTIVE INDEX GRATINGS IN RARE EARTH
DOPED ALKALINE EARTH GLASSES

Introduction

The observation of permanent laser-induced gratings in Eu^{3+} -doped glasses using four-wave-mixing (FWM) techniques was reported previously [38]. These gratings were produced by resonant excitation of the Eu^{3+} ions into the $^5\text{D}_2$ level. A model was proposed [38], [39] to explain the formation of these gratings based on a thermally-induced change in the local glass structure at the site of the Eu^{3+} ions. This results in the description of each electronic level of the Eu^{3+} ions in terms of a double-minimum potential well. The model assumes that the index of refraction of the material changes, depending on which potential well is occupied by the Eu^{3+} ions. Laser-induced refractive index gratings in Eu^{3+} -doped glasses are important when considering such glasses for optical devices. Several potential uses of these types of gratings have been demonstrated [40] including holographic storage, demultiplexing multifrequency laser beams, and beam-to-beam information transfer. In addition, silicate glasses can be made into fibers and thus devices based on laser-induced gratings in Eu^{3+} -doped silicate glasses can be used in fiber optics systems. The work reported here constitutes an extension of the previous investigations [38], [39] and describes the variation of the FWM signal intensity of a series of Eu^{3+} -doped silicate glasses with different divalent alkaline network modifier ions. The temperature dependence of the signal from one of the samples was measured and a theoretical explanation for the change in the refractive index associated with the double-minimum potential well model is developed.

Experimental Procedure and Results

The effect of different divalent network modifier ions on the characteristics of permanent laser-induced gratings was studied in five Eu^{3+} -doped silicate glasses with identical compositions except for one modifier ion which was changed through a series of divalent alkaline elements: Mg, Ca, Zn, Sr, Ba. The compositions of these glasses are listed in Table V.

Permanent laser-induced gratings were written in each sample at room temperature using crossed write beams from a c.w. argon-ion laser tuned to the 465.8 nm line in order to resonantly excite the $^5\text{D}_2$ level of the Eu^{3+} ions. The two write beams, each having a power of 30 mW, were focused to beam waists of 400 μm and superimposed inside the sample at a crossing angle of about 3° . The scattering efficiency of these gratings was measured using a He-Ne laser at 632.8 nm as the probe beam, which was focused to a waist of 200 μm and had a power of 5 mW. The experimental set-up was the same as shown in Figure 13. The writing time of the grating was about 15 min.

It was found that the scattering efficiency of the laser-induced gratings decreased as the mass of the modifier ion increased. Figure 21 displays a plot of the experimental values of the scattering efficiency versus the reduced mass of the modifier and the rare earth ion. The solid line represents the theoretical fit to the experimental data as explained in next section.

The temperature dependence of the laser-induced signal intensity in the Mg glass sample was measured at temperatures below and above room temperature. For low temperature measurements the sample was mounted in a cryostat and the temperature was controlled using a CTI-Cryogenics closed cycle helium refrigerator and a Lake Shore Cryotronics model 805 temperature controller. For high temperature measurements the sample was mounted in a resistance heated furnace with a Chromel-Alumel thermocouple. The laser-induced signal intensity is plotted versus temperature in Figure 22. As can be seen from the graph, the signal intensity increases as the temperature decreases. There is a change in slope

TABLE V
COMPOSITION OF GLASS SAMPLES INVESTIGATED

| Sample composition (mol %) | | | |
|----------------------------|---------------------|--------------------------------|----------------------------------|
| Sample | Network former | Network modifiers | Eu content |
| Mg glass | 65 SiO ₂ | 15 Na ₂ O 15 MgO | 5 Eu ₂ O ₃ |
| Ca glass | 65 SiO ₂ | 15 Na ₂ O 15 CaO | 5 Eu ₂ O ₃ |
| Zn glass | 65 SiO ₂ | 15 Na ₂ O 15 ZnO | 5 Eu ₂ O ₃ |
| Sr glass | 65 SiO ₂ | 15 Na ₂ O 15 SrO | 5 Eu ₂ O ₃ |
| Ba glass | 65 SiO ₂ | 15 Na ₂ O 15 BaO | 5 Eu ₂ O ₃ |

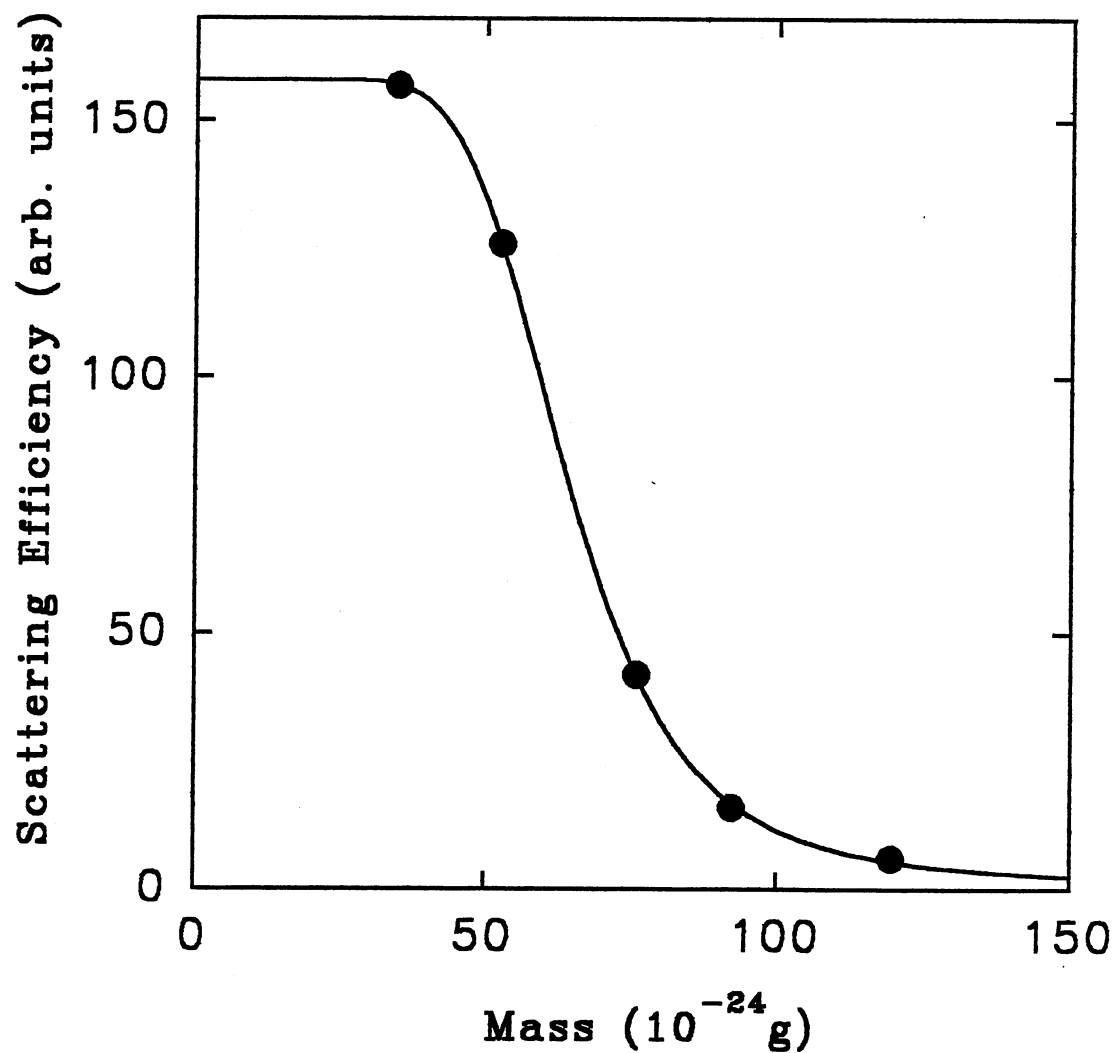


Figure 21. Scattering efficiency of the laser-induced permanent gratings as a function of the reduced mass of the alkaline earth modifier ion and rare earth ion. ●, experimental points; - theoretical prediction

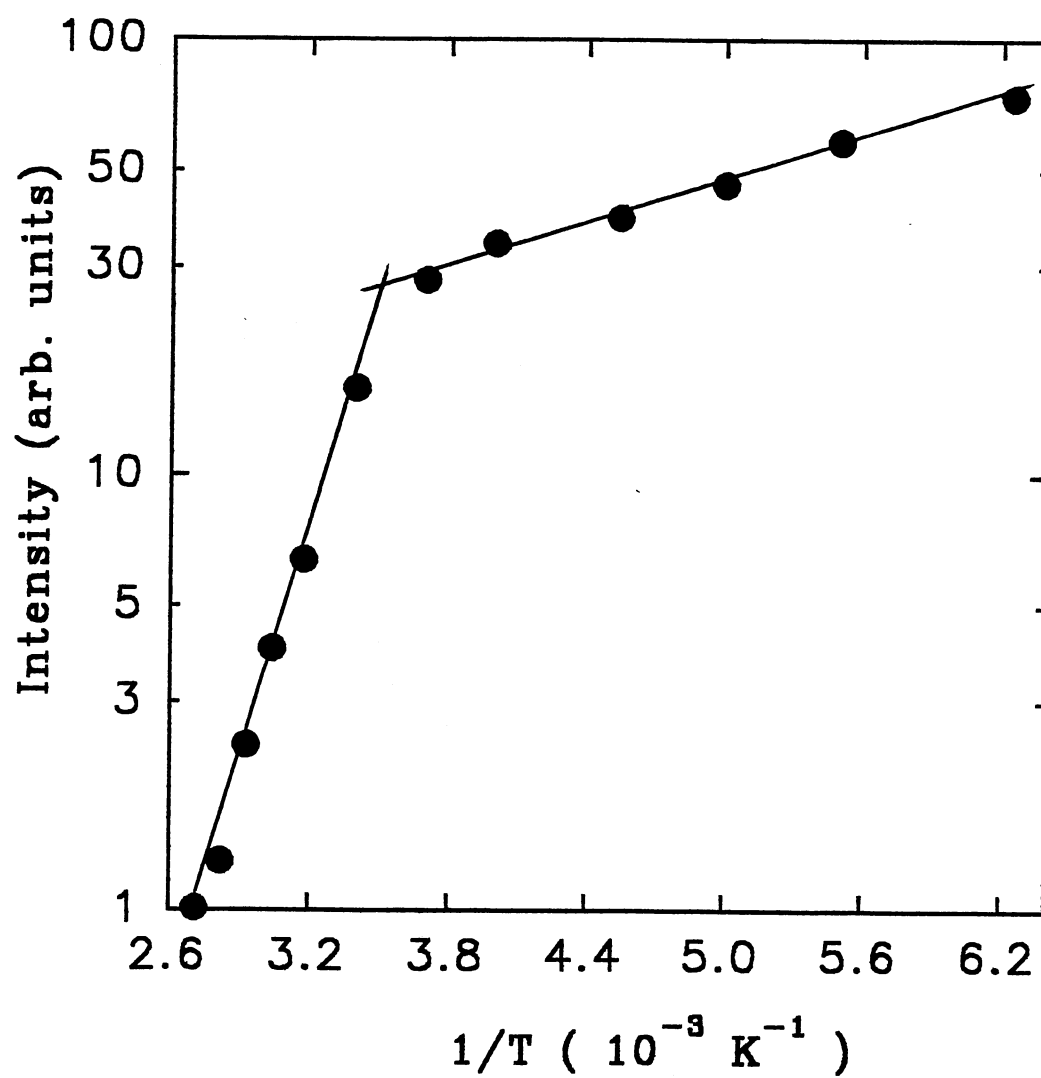


Figure 22. Intensity of the laser-induced signal in the Mg glass sample as a function of temperature

between high and low temperature regions. The solid lines in Figure 22 correspond to an exponential variation of the signal intensity given by [39]

$$I = I_0 \exp\left(\frac{\Delta}{k_B T}\right) \quad (116)$$

where Δ is an activation energy. The experimental values obtained for Δ are $2.72 \times 10^3 \text{ cm}^{-1}$ for the high temperature region and about $0.25 \times 10^3 \text{ cm}^{-1}$ for the low temperature region.

Interpretation of Results

The laser write beams directly excite the Eu^{3+} ions into the 5D_2 level. There is nonradiative relaxation to the 5D_0 level, followed by radiative emission in the orange, corresponding to the $^5D_0 - ^7F_1$ transition, and radiationless relaxation to the ground state 7F_0 . Figure 23 shows the relevant energy levels of the Eu^{3+} ion and the processes described above.

The model proposed previously to explain laser-induced permanent gratings is based on thermally-induced changes in the local glass structure at the site of the Eu^{3+} ions [39]. This model assumes that the network forming and modifier ions can arrange themselves in two possible equilibrium configurations leading to different local environments surrounding the Eu^{3+} ions. Each structural arrangement has a different refractive index. This results in double-minima potential wells for the electronic energy levels of the Eu^{3+} ions, as illustrated in Figure 24. The $^5D_2 - ^5D_0$ nonradiative relaxation of the Eu^{3+} ions produces high energy local vibrational modes [39]. It is assumed that the local heating generated by these vibrational modes is responsible for the laser-induced change in the local structure of the glass host [38]. This can be pictured as the Eu^{3+} ions moving from one potential well minimum to the other.

In the double-minimum potential well model the total index of refraction of the material is given by the sum of the contributions from both configurations [38]

$$n = n_I N_I + n_{II} N_{II} \quad (117)$$

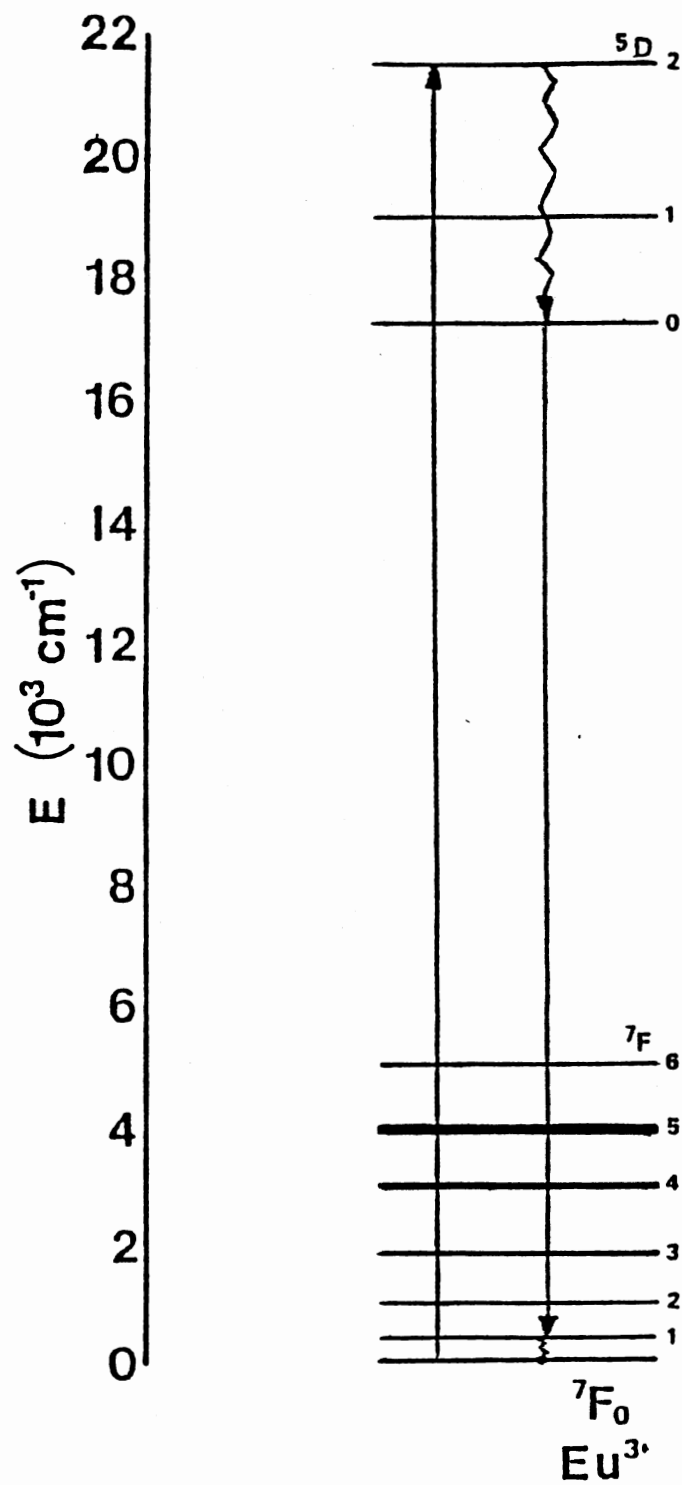


Figure 23. Diagram of the Eu^{3+} ion energy levels and relaxation processes relevant in this work

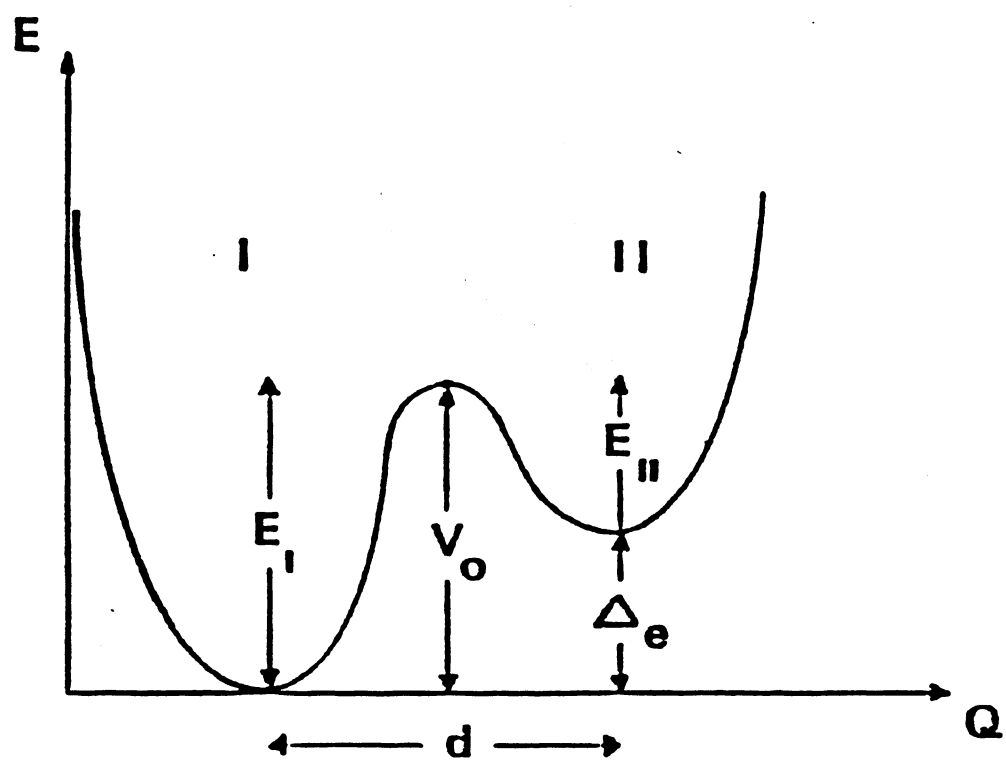


Figure 24. Double-minimum potential well model

where $N_{I(II)}$ is the population of well I(II) and $n_{I(II)}$ is the refractive index per ion in each well. The thermal equilibrium condition is written as [39]

$$\frac{N_I(\infty)}{N_{II}(\infty)} = \frac{\nu_{II}}{\nu_I} \exp\left(-\frac{\Delta_e}{k_B T}\right) \quad (118)$$

where $N_{I,II}(\infty)$ represents the population of each well after the system has reached equilibrium, $\nu_{I,II}$ is the attack frequency (the number of attempts an ion in well I (II) makes to surmount the potential height of that well) and Δ_e is the asymmetry (the difference in the minima of the two potential wells).

The intensity of the LIG signal is proportional to the square of the modulation of the refractive index [41]

$$I \propto |n_p - n_v|^2 \quad (119)$$

where n_p and n_v are the index of refraction of the peak and valley regions of the grating, respectively, and they can be written as [39]

$$\begin{aligned} n_p &= n_I N_{Ip}(\infty) + n_{II} N_{IIp}(\infty) \\ n_v &= n_I N_{Iv}(\infty) \end{aligned} \quad (120)$$

The subscripts p and v refer to the peak and valley regions of the LIG and I and II refer to the potential well occupied. Here it is assumed that the ions in the valley region of the grating remain in well I at all times.

Using Eq. 118 and the condition that the total population of the wells must remain constant, the LIG effective scattering efficiency is written as [39]

$$\eta_{eff} \equiv \frac{I}{N_I^2(0)} \propto \frac{|\Delta n_{II-I}|^2}{\left[1 + \frac{\nu_{II}}{\nu_I} \exp\left(-\frac{\Delta_e}{k_B T}\right)\right]^2} \quad (121)$$

where $N_I(0)$ is the population of well I before excitation (initially all ions are assumed [39] to be in well I) and Δn_{II-I} is the change in refractive index per ion. Using the mathematical formalism developed to describe a double-minimum potential well, Δ_e can be written as [39]

$$\Delta_e = \frac{\hbar}{\tan \Theta} \sqrt{\frac{k}{m}} \exp\left[-d \left(\frac{2mV_0}{\hbar^2}\right)^{1/2}\right] \quad (122)$$

where $\tan\Theta = \Delta_0/\Delta_e$, Δ_0 being the coupling energy [39] (i.e., $\Delta_0 = 2\langle\varphi_1 | H | \varphi_2\rangle$, $|\varphi_1\rangle$ and $|\varphi_2\rangle$ are the ground states of each well and $H=H_0+W$, H_0 being the Hamiltonian of the unperturbed system and W a perturbation which couples states $|\varphi_1\rangle$ and $|\varphi_2\rangle$), k is the force constant of the initial configuration, m is the mass of the ion populating the well, d is the distance between the minima of well I and well II and V_0 the potential barrier between the two wells. Inserting Eq. 122 into Eq. 121, the effective scattering efficiency of the LIG is given by

$$\eta \propto \frac{|\Delta n_{II-I}|^2}{\left(1 + \frac{\nu_{II}}{\nu_I} \exp \left\{ \frac{-\hbar(k/m)^{1/2}}{k_B T \tan \Theta} \exp \left[-d \left(2mV_0/\hbar^2 \right)^{1/2} \right] \right\} \right)^2} \quad (123)$$

The value used for m in Eq. 123 was the reduced mass of the divalent modifier ion and rare earth ion for each of the samples investigated. Although, realistically there are many ions moving and thus contributing to the formation of the two equilibrium configurations, we consider in this model that the main source of the double-minimum potential well is the change in position of the divalent modifier ion and the rare-earth ion. The change in position of all other ions is considered to be very small, so that their contribution to the double-minimum potential well is negligible. Equation 123 was fit to the experimental values of the scattering efficiency treating $|\Delta n_{II-I}|^2$, ν_{II}/ν_I , $\hbar k^{1/2}/(k_B T \tan \Theta)$, and $d(2V_0/\hbar^2)^{1/2}$ as adjustable parameters. The solid line in Figure 21 represents the best fit to the experimental data where the values found for the adjustable parameters are:

$$\begin{aligned} |\Delta n_{II-I}|^2 &= (1.58 \pm 0.05) \times 10^{-44}, \\ \nu_{II}/\nu_I &= 15.6 \pm 0.5, \\ \hbar k^{1/2}/(k_B T \tan \Theta) &= (2.25 \pm 0.10) \times 10^{-10} g^{1/2}, \\ d(2V_0/\hbar^2)^{1/2} &= (2.55 \pm 0.10) \times 10^{11} g^{-1/2}. \end{aligned}$$

The sensitivity of the fit to these values of the adjustable parameters is expressed by the \pm error bars given above.

The constant of proportionality in Eq. 123 was calculated using the fact that the scattering efficiency of the FWM signal is given, to a first approximation, by[41]

$$\eta = \exp(-2\alpha_0\Gamma) \pi^2 \Gamma^2 (\Delta n_{total})^2 / \lambda^2. \quad (124)$$

Here $\Gamma = D / \cos 2\theta$, where D is the grating thickness, 2θ is the angle between the write beams in the sample, λ is wavelength of the write beams, Δn_{total} represents the modulation of the refractive index of the sample and α_0 is the absorption coefficient of the sample at the write beam frequency.

The values of the adjustable parameters were used in Eqs. 122 and 118 to calculate the difference in the minima of the two wells, Δ_e , the population of well I before excitation, $N_I(0)$, and the population of each well after the system has reached equilibrium, $N_{I,II}(\infty)$, for each of the samples investigated in this work. The values of these parameters are listed in Table VI. It is observed that the asymmetry decreases as the mass of the divalent modifier ion increases. This same trend was reported [39] in a series of silicate glasses with different monovalent modifier ions and was attributed to the fact that the glass becomes more ordered as the radius of the modifier ion increases and therefore the possibility for multiple configurations decreases.

The decrease in the difference between the two potential minima in the samples with heavier modifier ions is an indication of the fact that there is less thermally-induced change in the local glass structure. Because of this, it is more difficult to trap ions in well II in these samples. This is shown in Table VI by the decrease in the ratio $N_{II}(\infty)/N_I(0)$ as the mass of the modifier ion increases.

Using the value obtained for the last adjustable parameter and the fact that V_0 must be at least as large as $\Delta_e/2$, it is possible to approximate [39] the distance, d , between the two potential minima, which is a measure of the average distance the ions move. This distance varies from 0.04 Å for the Mg glass sample to 0.12 Å for the Ba glass sample, as listed in Table VI. These small values for d indicate that, as individual ions or groups of ions move between the two possible equilibrium configurations, I and II, the effect on the average configuration coordinate is very small.

The change in refractive index per ion is 1.26×10^{-22} , and considering the number of ions that accumulate in well II, which is of the order of 1×10^{16} , the total change in the refractive index of the material is 1.26×10^{-6} . This is consistent

TABLE VI
DOUBLE-MINIMUM POTENTIAL WELL
PARAMETERS

| Sample | Δ_e | $N_I(0)$ | $N_I(\infty)$ | $N_{II}(\infty)$ | $\frac{N_{II}(\infty)}{N_I(0)}$ | d |
|----------|----------------------------------|------------------|------------------|------------------|---------------------------------|------|
| | ($\times 10^3 \text{cm}^{-1}$) | $\times 10^{16}$ | $\times 10^{16}$ | $\times 10^{16}$ | | (Å) |
| Mg glass | 1.72 | 6.84 | 0.02 | 6.82 | 0.99 | 0.04 |
| Ca glass | 0.99 | 4.59 | 0.49 | 4.10 | 0.89 | 0.06 |
| Zn glass | 0.57 | 5.25 | 2.55 | 2.70 | 0.51 | 0.08 |
| Sr glass | 0.41 | 7.59 | 5.11 | 2.48 | 0.33 | 0.09 |
| Ba glass | 0.26 | 5.52 | 4.50 | 1.02 | 0.18 | 0.12 |

with the results obtained for silicate glasses with monovalent modifier ions in an earlier paper [39].

As reported in the previous section, the activation energy for the Mg glass sample for the high temperature region was found to be $2.72 \times 10^3 \text{ cm}^{-1}$ and since the activation energy is twice the asymmetry [39], this would give an asymmetry of $1.36 \times 10^3 \text{ cm}^{-1}$. This value is slightly lower than the calculated value for Δ_e listed in Table VI. However, considering the simplicity of the model used here to describe a complex physical system, the experimental and calculated values for Δ_e are close enough. Similar results were obtained for the glasses with monovalent modifier ions [46].

One important assumption made in the double-minimum potential well model is that the refractive index of the material is different for the two possible local configurations, that is n depends on which potential minimum is occupied by the Eu^{3+} ions [38,39]. This change in the refractive index needs to be theoretically explained and evaluated.

Starting from the Clausius-Mossotti equation, the change in refractive index, Δn_{total} , between the two configurations can be related to the change in the polarizability, $\Delta \alpha_p$, of the Eu^{3+} ions in configuration II as compared to configuration I by [42]

$$\Delta n_{total} = \frac{2\pi}{n} f_L^2 N_{ex} \Delta \alpha_p \quad (125)$$

where $f_L = (n^2 + 2)/3$ is the Lorentz field correction and N_{ex} is the number density of the Eu^{3+} ions in configuration II. Using the numerical values calculated from our experimental data for the change in refractive index per ion, Δn_{II-I} , the number of ions that have moved to well II, $N_{II}(\infty)$, and the volume of interaction of the laser beams inside the sample, the change in polarizability, $\Delta \alpha_p$, is calculated to be 0.0134 \AA^3 .

For a theoretical evaluation of the change in polarizability we used the model developed by Powell, et al. [37] to calculate the change in polarizability of the $^4\text{F}_{3/2}$ excited state of Nd^{3+} compared to that of the $^4\text{I}_{9/2}$ ground state for a variety of host materials. They considered that the Nd^{3+} ion was a multilevel system and

that the laser beams could interact with all possible transitions between those levels. Having recognized that the 4f - 4f transitions "borrow" intensity from the 4f - 5d and 4f - ng transitions, they estimated that the main contribution to the change in the polarizability of the Nd³⁺ ion was due to the 4f - 5d interactions.

Here we consider that the change in polarizability of the Eu³⁺ ions in configuration II as compared to configuration I is mainly due to the 4f - 5d transitions which are far from resonance and given by [37]

$$\Delta\alpha_p = \frac{3\nu_0^{(5d)}\alpha_{FS}}{7\pi} \left[\frac{1}{(\nu_0^{(5d)} - \nu_{ex})^2 - \nu^2} - \frac{1}{(\nu_0^{(5d)})^2 - \nu^2} \right] |\langle 4f | r | 5d \rangle|^2 \quad (126)$$

where $\nu_0^{(5d)}$ is the average energy of the 4f⁵5d states, ν is the energy of the laser photons, ν_{ex} is the energy difference between the two equilibrium configurations, I and II, and α_{FS} is the fine structure constant.

Figure 25 shows the relevant energy levels of the Eu³⁺ ions with the two possible local configurations of the glass host, I and II. The numerical values used in Eq. 126 were the free-ion values [37]. The lowest 4f⁵5d level of the Eu³⁺ free ion is known [43] to be at 85,500 cm⁻¹ and, due to the 20,000 cm⁻¹ splitting of the 5d level, the median energy of the 4f⁵5d manifold is at about 95,500 cm⁻¹. The value of the radial integral $\langle 4f | r | 5d \rangle$ for the Eu³⁺ free ion is [44] 0.41 Å and $\alpha_{FS} = 1/137$. Using the value of $\Delta\alpha_p$ calculated from the experimental results and Eq. 125 in Eq. 126, the energy difference between the two configurations is found to be $\nu_{ex} = 3.14 \times 10^3$ cm⁻¹.

Since the difference between the ground state energy of the Eu³⁺ ion in configuration II as compared to configuration I was calculated to be 1.72×10^3 cm⁻¹ for the Mg glass sample, as listed in Table VI, the remaining energy difference between the two configurations is accounted for by a shift of 1.42×10^3 cm⁻¹ in the 5d levels of configuration II as compared to configuration I. From Table VI, it is seen that the shift in the ground state energy becomes smaller as the mass of the modifier ion increases. This would lead to increasing shifts in the 5d levels, from 1.42×10^3 cm⁻¹ for the Mg glass sample to 2.88×10^3 cm⁻¹ for the Ba glass sample.

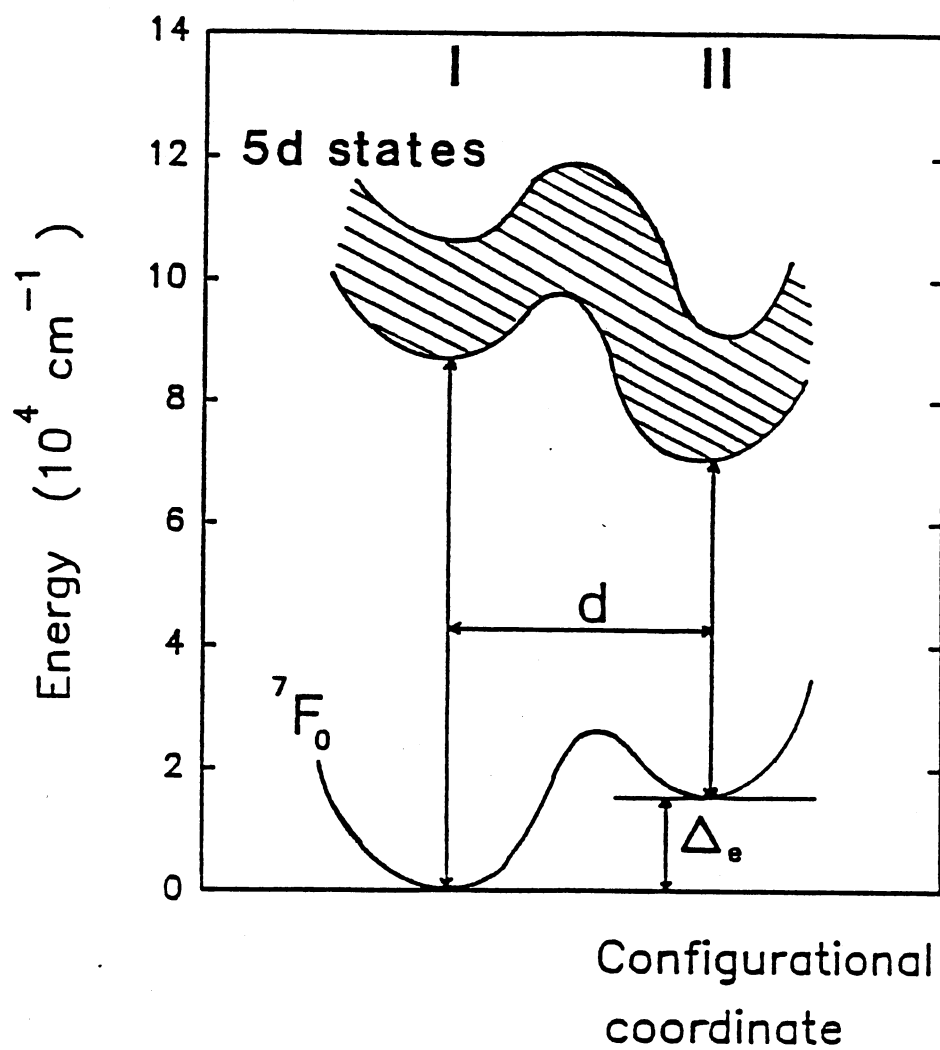


Figure 25. Configuration coordinate diagram showing the relevant energy levels of the Eu^{3+} ion with the two possible local configurations of the glass host, I and II

The energy difference between the two equilibrium configurations was calculated based on the free-ion value of the radial integral $\langle 4f | r | 5d \rangle$. The value of this integral will be smaller [37,44] for the Eu^{3+} ions incorporated into a host environment. This, in turn, would mean that the energy shifts from one configuration to the other may be somewhat larger than those calculated using the free-ion value for the radial integral. Even then, the results predicted by this model are reasonable, since site-selective spectroscopy has shown [45] energy shifts in the 5d level of about $6,000 \text{ cm}^{-1}$ from one site of the impurity ion to another in a glass host. However, it is also true that the value of the radial integral can change significantly due to a change in local environment [37]. It is impossible to tell from these results whether the change in the radial integral or the change in the position of the 5d level makes the dominant contribution to the change in the polarizability. Both types of changes will contribute to the observed results.

Discussion

Unfortunately, there is still very little known on the atomic scale concerning the local environment of rare earth ions doped into glass hosts. It is thought that ions such as Eu^{3+} in silicate glasses occupy interstitial sites and distort the local environment of the host by their Coulomb attraction of the nonbridging oxygen ions. This results in local environments with high nearest neighbor coordination numbers caused by the distortion of the rare earth ion on its surroundings. In producing this distortion, the trivalent rare earth ion is in competition with the modifier ions of the host in attracting the nonbridging oxygen ions. Modifier cations in the second coordination sphere increase the rigidity of the host, thus hindering the free formation of the rare earth ion environment. The success of this competition for attracting the nonbridging oxygen ions is determined by the relative field strengths of the rare earth and modifier ions. Thus, the larger the charge-to-radius ratio is for the rare earth ion compared to that of the modifier ions, the more the rare earth ion will be able to distort its surroundings.

The above discussion can be used to understand the results listed in Table VI. The asymmetry factor Δ_e for the double potential well is a measure of the ability of the rare earth ion to distort its local environment. If the rare earth ion is able to freely distort its environment, it will form a very similar local environment at each site resulting in a small value for the asymmetry parameter. This is reflected in Table VI which shows that the hosts with large modifier ions and thus low effective fields have small values for Δ_e whereas the hosts having small modifier ions with high electric fields have large values of Δ_e . This is also consistent with the results published previously for hosts with monovalent modifier ions [39]. The Δ_e values are larger for the glasses with divalent modifier ions compared to those found in similar glasses with monovalent modifier ions due to the higher local field strength of the former.

CHAPTER IV

CONCLUSIONS

The results presented in Chapter II provide a characterization of the energy transfer and migration processes in Tm,Ho:YAG, Tm:YAG and Cr,Tm,Er:YAG crystals. This study has characterized the individual ion-ion interaction processes separately and has shown how their combined effects lead to the efficient Tm sensitization of Ho luminescence that has been observed experimentally. Spatial energy migration was found to occur in the Tm 3F_4 level. The results of LIG spectroscopy show that this process occurs through a long mean-free-path random walk in which the migrating excitation is scattered by acoustic phonons. The ion-ion interaction rate causing each step in the random walk is accurately described by an electric dipole-dipole mechanism. This decreases at low temperatures as the spectral overlap that characterizes the resonant interaction between neighboring ions decreases. The temperature and Tm ion concentration dependences of the results are accurately described by this model. The overall Tm-Ho energy transfer rate was calculated using the excitation migration parameters described above. A simple model assuming the Ho ions act as traps for the migrating Tm ion excitation gives a reasonable agreement with the transfer rate measured from fluorescence spectral dynamics. The trapping step is consistent with the prediction of an electric dipole-dipole interaction mechanism that de-excites the Tm ion in the 3F_4 level and excites the Ho ion to the 5I_7 level. The rate of this interaction step is greater than the rate of the Tm-Tm migration step, and thus the overall transfer is a diffusion-limited process. No energy transfer from Tm to Er was detected in sample 6 for the excitation conditions used in this work. In addition, the parameters for the Tm migration process in this sample are not consistent with those obtained for the Tm:YAG and Tm,Ho:YAG samples. More investigations are needed to determine

the nature of the excitation scattering mechanism dominant in this sample and to characterize the role of the Er ions as scattering centers vis-a-vis that of the Ho ions as traps in Tm,Ho:YAG.

In Chapter III laser induced grating spectroscopy was used to investigate the properties of permanent refractive index gratings in silicate glasses. Using the double-minimum potential well model to explain permanent laser-induced gratings in Eu^{3+} -doped glasses, a theoretical explanation was developed for the change in the refractive index for different local structural configurations of the material. The change in the refractive index was related to the change in the polarizability of the Eu^{3+} ions in the two types of configuration, which in turn, was calculated from the experimental data to be $\Delta\alpha_p = 0.0134 \text{ \AA}^3$. The change in refractive index per ion was obtained as an adjustable parameter from fitting Eq. 123 to the experimental data and therefore has the same value for all glass samples investigated here. The total change in refractive index varies from host to host due to the fact that the number of ions moving from configuration I to configuration II is host dependent as shown in Table VI. However, the actual value of Δn_{II-I} may also change a little from one glass host to another. The theoretical model used here can accurately explain all of the observed results by assuming that this change is very small so that its contribution to the change in total refractive index is negligible.

On the basis of free-ion wave-functions and the assumption that the 4f-5d transitions make the dominant contribution to the change in polarizability between the two configurations, a shift in transition energy from configuration I to configuration II of $3.14 \times 10^3 \text{ cm}^{-1}$ was calculated. This is a physically reasonable energy level shift but the actual value may be different due to the change in the value of the radial integral between the two configurations. Previous results on other types of samples indicate that this latter effect makes the dominant contribution to the polarizability change in different host environments [37]. It is interesting to note that the value of Δn_{II-I} found for Pr^{3+} -doped glasses is the same as that found for Eu^{3+} in the same hosts [46]. Since the 5d levels for Pr^{3+} are at lower energies than those of Eu^{3+} , these results imply that the change in radial integral

is more important than the change in the position of the 5d levels in determining the polarizability of the rare earth ions in glass hosts.

Although the results described here extend our understanding of the formation of laser-induced permanent gratings in rare earth-doped glasses, there are still several aspects of this phenomenon that require further investigation. The exact nature of the local surroundings of the rare earth ion on the atomic scale is still not known and finding the right rare earth-host glass combination to optimize this effect is still an important area of research.

BIBLIOGRAPHY

1. Fan, T.Y., G. Huber, R.L. Byer, and P. Mitzscherlich, *IEEE J. Quantum. Electron.* 24, 924 (1988).
2. Tyminski, J.K., D.M. Franich, and M. Kokta, *J. Appl. Phys.* 65, 3181 (1989).
3. Armagan, G., A.M. Buoncristiani, and B. Di Bartolo, *J. Luminescence* 48-49, 171 (1991); G. Armagan, A.M. Buoncristiani, and B. Di Bartolo, *Opt. Mater.* 1, 11 (1992).
4. Quarles, G.J., A. Rosenbaum, C.L. Marquardt, and L. Esterowitz, *Appl. Phys. Lett.* 55, 1062 (1989).
5. Jani, M.J., R.R. Reeves, R.C. Powell, G.J. Quarles, and L. Esterowitz, *J. Opt. Soc. Am. B* 8, 741 (1991).
6. Brenier, A., J. Rubin, R. Moncorge, and C. Pedrini, *J. Phys. France* 50, 1463 (1989).
7. Payne, S.A., L.K. Smith, W.L. Kway, and W.F. Krupke, *J. Phys. Condens. Matter* (to be published).
8. Powell, R.C. and G. Blasse, in Structure and Bonding, Vol. 42, edited by J.D. Dunitz, J.B. Goodenough, P. Hemmerich, J.A. Ibers, C.K. Jorgensen, J.B. Neilands, D. Reinen and R.J.P. Williams (Springer-Verlag, Berlin, 1980), p. 43.
9. Forster, T. , *Ann. Phys.* 2, 55 (1948); *Z. Naturforsch.* 49, 321 (1949).
10. Dexter, D.L., *J. Chem. Phys.* 21, 836 (1953).
11. Di Bartolo, B., Optical Interactions in Solids (Wiley, New York, 1968).
12. Di Bartolo, B., Energy Transfer Processes in Condensed Matter (Plenum Press, New York, 1984).
13. Di Bartolo, B., Optical Properties of Ions in Solids (Plenum Press, New York, 1975).
14. Powell, R.C., B. Di Bartolo, B. Birang, and C.S. Naiman, *Phys. Rev.* 155, 296 (1967).

15. Zverev, G.M., G.Y. Kolodnyi, and A.M. Onishchenko, Sov. Phys. JETP 30, 435 (1970).
16. Burshtein, A.I., Sov. Phys. JETP, 35, 882 (1972).
17. Burshtein, A.I., Sov. Phys. JETP, 57, 1165 (1983).
18. Artamonova, M.V., C.M. Briskina, A.I. Burshtein, L.D. Zusman, and A.G. Skleznev, Sov. Phys. JETP, 35, 457 (1972).
19. Bondar, I.A., A.I. Burshtein, A.V. Krutikov, L.P. Mezentsева, V.V. Osiko, V.P. Sakun, V.A. Smirnov, and I.A. Shcherbakov, Sov. Phys. JETP, 54, 45 (1981).
20. Huber, D.L., Phys. Rev. B 20, 2307 (1979).
21. Inokuti, M., and F. Hirayama, J. Chem. Phys. 43, 1978 (1965).
22. Huber, D.L., Phys. Rev. B 20, 5333 (1979).
23. Huber, D.L., in Laser Spectroscopy of Solids, vol. 49, edited by W.M. Yen and P.M. Selzer (Springer-Verlag, Berlin, 1981).
24. Trlifaj, M., Czech. J. Phys. 8, 510 (1958).
25. Blumen, A., and R. Silbey, J. Chem. Phys. 70, 3707 (1979).
26. Salcedo, J.R., A.E. Siegman, D.D. Dlott, and M.D. Fayer, Phys. Rev. Lett. 41, 131 (1978).
27. Lawson, C.M., R.C. Powell and W.K. Zwickler, Phys. Rev. B 26, 4836 (1982); Phys. Rev. Lett. 46, 1020 (1981); R.C. Powell, J.K. Tyminski, A.M. Ghazzawi, and C.M. Lawson, IEEE J. Quantum. Electron. QE-22, 1360 (1986).
28. Morgan, G.P., S. Chen, and W.M. Yen, IEEE J. Quantum Electron. QE-22, 1360 (1986).
29. Kenkre, V.M., in Exciton Dynamics in Molecular Crystals and Aggregates, edited by G. Hohler (Springer-Verlag, Berlin, 1982).
30. Kenkre, V.M., Phys. Rev. B 18, 4064 (1978).
31. Wong, Y.M. and V.M. Kenkre, Phys. Rev. B 22, 3072 (1980).
32. Kenkre, V.M. and D. Schmid, Phys. Rev. B 31, 2430 (1985).
33. Kenkre, V.M., V. Ern, and A. Fort, Phys. Rev. B 28, 598 (1983).
34. Chandrasekhar, S., Rev. Mod. Phys. 15, 1 (1943).

35. Agranovich, V.M., and M.D. Galanin, Electronic Excitation Energy Transfer in Condensed Matter, (North-Holland, Amsterdam, 1982).
36. French, V.A., R.R. Petrin, R.C. Powell, and M. Kokta, Phys. Rev. B 46, 8018 (1992).
37. Powell, R.C., S.A. Payne, L.L. Chase, and G.D. Wilke, Phys. Rev. B 41, 8593 (1990).
38. Durville, F.M., E.G. Behrens, and R.C. Powell, Phys. Rev. B 34, 4213 (1986); F.M. Durville, E.G. Behrens, and R.C. Powell, Phys. Rev. B 35, 4109 (1987); E.G. Behrens, F.M. Durville, and R.C. Powell, Opt. Lett. 11, 653 (1986).
39. Behrens, E.G., F.M. Durville, and R.C. Powell, Phys. Rev. B 39, 6076 (1989).
40. Behrens, E.G., R.C. Powell, and D.H. Blackburn, Appl. Opt. 29, 1619 (1990).
41. Kogelnik, H., Bell System Tech. J. 48, 2909 (1969).
42. Weaver, S.C., and S.A. Payne, Phys. Rev. 40, 10727 (1989).
43. Brewer, L., J. Opt. Soc. Am. 61, 1666 (1971).
44. Krupke, W.F., Phys. Rev. 145, 325 (1966).
45. Arbuzov, V.I., L.V. Viktorov, E.I. Galant, A.K. Przhhevuskii, and M.N. Tolstoi, Sov. J. Chem. Glass 8, 223 (1982).
46. Behrens, E.G., R.C. Powell, and D.H. Blackburn, J. Opt. Soc. Am. B 7, 1437 (1990).

VITA

VALENTINA A. FRENCH

Candidate for the Degree of

Doctor of Philosophy

Thesis: LASER INDUCED GRATING SPECTROSCOPY OF RARE EARTH
IONS IN SOLIDS

Major field: Physics

Biographical:

Personal Data: Born in Ploiesti, Romania, daughter of Valentin and Florica Popescu. Married to Robert French.

Education: Received Bachelor of Science Degree in Physics from University of Bucharest, Romania in 1981; received Master of Science Degree in Physics from Oklahoma State University, Stillwater, Oklahoma in 1987; completed requirements for the Doctor of Philosophy Degree at Oklahoma State University, Stillwater, Oklahoma in December, 1992.